

Applying the Worldvolume Hybrid Monte Carlo method to the Hubbard model away from half filling

Masafumi Fukuma^{1*} and Yusuke Namekawa^{2†}

¹*Department of Physics, Kyoto University, Kyoto 606-8502, Japan*

²*Department of Computer Science, Fukuyama University, Hiroshima 729-0292, Japan*

Abstract

The Worldvolume Hybrid Monte Carlo (WV-HMC) method [arXiv:2012.08468] is an efficient algorithm for addressing the numerical sign problem at moderate computational cost. It mitigates the sign problem while avoiding the ergodicity issues inherent in approaches based on Lefschetz thimbles. In this study, we apply WV-HMC to the two-dimensional Hubbard model doped away from half filling, which is known to suffer from a severe sign problem. We compute the number density and the energy density on lattices of size 6×6 and 8×8 at temperature $T/t = 1/6.4 \simeq 0.156$ and interaction strength $U/t = 8.0$, using Trotter number $N_t = 20$ (Trotter step $\epsilon = 0.32$). Our results demonstrate that WV-HMC remains effective even in parameter regimes where standard (non-thimble) determinant quantum Monte Carlo methods fail. In this work, fermion matrix inversions are performed using direct solvers, leading to a computational cost of $O(N^3)$, where N denotes the number of degrees of freedom and is proportional to the spacetime lattice volume. An alternative algorithm employing pseudofermions and iterative solvers, which reduces the cost to $O(N^2)$ at the expense of careful parameter tuning, will be discussed in a separate publication.

*E-mail address: fukuma@gauge.scphys.kyoto-u.ac.jp

†E-mail address: namekawa@fukuyama-u.ac.jp

Contents

1	Introduction	1
2	Worldvolume Hybrid Monte Carlo (WV-HMC)	3
3	Path-integral representation of the Hubbard model	10
3.1	The Hubbard model	10
3.2	Bosonization	13
4	Applying WV-HMC to the Hubbard model	15
4.1	Flow equations	15
4.2	Observables	16
5	Results on the one-dimensional Hubbard model	18
6	Results on the two-dimensional Hubbard model	19
6.1	Computational cost scaling	19
6.2	Tuning of α	19
6.3	Sign problem after α tuning	20
6.4	Results on the 6×6 spatial lattice	21
6.5	Results on the 8×8 spatial lattice	22
7	Conclusions and outlook	23

1. Introduction

The numerical sign problem arises in a variety of physically important systems, including quantum chromodynamics (QCD) at finite density, strongly correlated electron systems, and real-time dynamics of quantum many-body systems. Among recent efforts to develop versatile algorithms to address this problem, the Lefschetz thimble method [1–9] has emerged as a promising approach. This method continuously deforms the original integration surface $\Sigma_0 = \mathbb{R}^N$ (with N denoting the number of degrees of freedom) into a submanifold Σ within the complexified space \mathbb{C}^N . The deformed surface asymptotically approaches a union of Lefschetz thimbles, on each of which the imaginary part of the action is constant, thereby suppressing phase fluctuations of the integrand and alleviating the sign problem. However,

the presence of infinitely high potential barriers between adjacent thimbles leads to an ergodicity problem. This issue was resolved by performing (parallel) tempering with respect to the deformation parameter, as implemented in the tempered Lefschetz thimble (TLT) method [10, 11] (see also Ref. [12]). A principal drawback of this approach is its high computational cost, primarily due to the need to evaluate the Jacobian of the deformation at every exchange of configurations, in order to take into account the difference between the volume elements of the replicas.

The *Worldvolume Hybrid Monte Carlo* (WV-HMC) method [13] (see also Refs. [14–18]) was then introduced to address this issue. In this algorithm, Hybrid Monte Carlo (HMC) updates are performed over a continuous union of deformed integration surfaces. This region is referred to as the *worldvolume* because it can be viewed as the orbit of the integration surface in the target space \mathbb{C}^N (or as the orbit in $G^{\mathbb{C}}$ when the original integration space Σ_0 is a compact Lie group G [16]). The sampling is performed over the tangent bundle of the worldvolume, which has a natural symplectic structure. We no longer need to compute the Jacobian in configuration generation because the phase-space volume element does not change provided that we employ a symplectic integrator (such as RATTLE [19, 20]) in molecular dynamics.

The Hubbard model has long been regarded as one of the most important models in condensed matter physics, as it provides a minimal description of the essential competition between electron itinerancy and local Coulomb repulsion in solids. The model is also highly relevant to particle physics, because its bosonized form (obtained through the Hubbard–Stratonovich transformation) shares structural similarities with that in finite-density QCD. However, the model suffers from a severe sign problem when it is doped away from half filling. A variety of numerical methods have been developed to address this issue, including variational Monte Carlo [21–24], constrained-path auxiliary-field quantum Monte Carlo [25, 26], as well as more recent approaches such as the Lefschetz thimble method [27–32], the TLT method [12], tensor renormalization group techniques [33, 34], complex-valued neural networks [35], constant path-integral contour shifts [36], and equivariant normalizing flows [37].

In this paper, we apply the WV-HMC method to the doped Hubbard model. We compute the number and energy densities on 6×6 and 8×8 lattices at temperature $T/t = 1/6.4 \simeq 0.156$ and interaction strength $U/t = 8.0$ for various values of the chemical potential μ , where t denotes the hopping amplitude. The temporal direction is discretized using Trotter number $N_t = 20$ (corresponding to Trotter step $\epsilon = 0.32$).¹ We compare our results with those obtained using ALF (Algorithms for Lattice Fermions) [39, 40], a highly efficient, state-

¹The continuum limit $\epsilon \rightarrow 0$ is discussed in a subsequent paper [38], where a machinery is developed to enable simulations on larger spacetime lattices.

of-the-art, non-thimble determinant quantum Monte Carlo (DQMC) framework widely used in the condensed-matter community. In our implementation, we employ direct solvers for inverting fermion matrices, which leads to a computational cost scaling as $O(N^3)$, where N is the number of degrees of freedom and is proportional to the spacetime lattice volume. An alternative formulation using pseudofermions and iterative solvers, which reduces the cost to $O(N^2)$ at the expense of careful parameter tuning, will be presented in a separate publication.

This paper is organized as follows. Section 2 reviews the WV-HMC algorithm, in which the computation of observables are reduced to phase-space integrals over the tangent bundle of the worldvolume, which carries a natural symplectic structure. Section 3 presents a path-integral formulation of the Hubbard model that is well suited for WV-HMC simulations. Section 4 provides the explicit formulas used in applying WV-HMC to the Hubbard model. Section 5 reports numerical results for the one-dimensional doped Hubbard model at high temperature, confirming that WV-HMC reproduces the exact values with high accuracy. Section 6 presents simulations of the two-dimensional doped Hubbard model at low temperature, where the computational cost is shown to scale as $O(N^3)$. The number and energy densities are estimated on 6×6 and 8×8 spatial lattices using the physical parameters specified above, and are shown to yield statistically controlled results even in parameter regions where conventional DQMC fails due to severe sign problems. Section 7 is devoted to conclusions and outlook, with particular emphasis on extending the simulations to larger spacetime volumes. Preliminary results of this study were reported at Lattice conferences [17, 18].

2. Worldvolume Hybrid Monte Carlo (WV-HMC)

In this section, we give a brief introduction to the WV-HMC method. See Refs. [13–16] for details.

Our aim is to numerically estimate the expectation value of an observable $\mathcal{O}(x)$ defined by a path integral over the configuration space $\mathbb{R}^N = \{x\}$,

$$\langle \mathcal{O} \rangle \equiv \frac{\int_{\mathbb{R}^N} dx e^{-S(x)} \mathcal{O}(x)}{\int_{\mathbb{R}^N} dx e^{-S(x)}}, \quad (2.1)$$

where $S(x) \in \mathbb{C}$ is a complex-valued action and $dx \equiv dx^1 \wedge \cdots \wedge dx^N$ is the flat measure. Since the Boltzmann weight $e^{-S(x)} / \int_{\mathbb{R}^N} dx e^{-S(x)}$ does not serve as a real and positive probability density, Monte Carlo methods based on importance sampling cannot be directly applied. A standard workaround is the so-called naive reweighting method, which defines a sampling

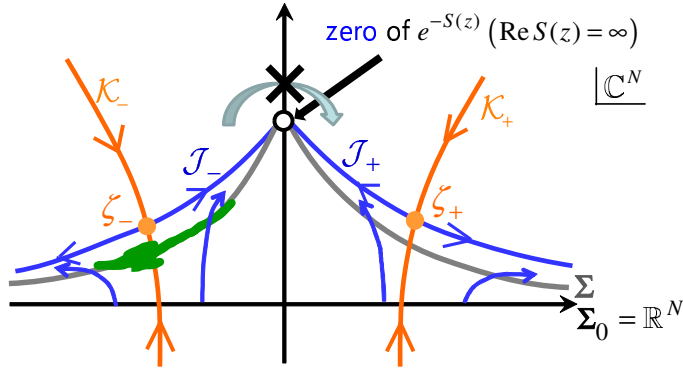


Figure 1: Lefschetz thimble method and its ergodicity problem (figure adapted from Ref. [15]). The original integration surface $\Sigma_0 = \mathbb{R}^N$ is deformed into Σ within \mathbb{C}^N . \mathcal{J}_\pm (\mathcal{K}_\pm) are Lefschetz thimbles (anti-thimbles) associated with critical points ζ_\pm . A Monte Carlo walker in the vicinity of one thimble \mathcal{J}_- cannot move to that of another thimble \mathcal{J}_+ due to the infinitely high potential barrier at zeros of $e^{-S(z)}$.

measure using the real part of the action and expresses $\langle \mathcal{O} \rangle$ as a ratio of reweighted averages:

$$\langle \mathcal{O} \rangle = \frac{\int_{\mathbb{R}^N} dx e^{-\text{Re } S(x)} e^{-i\text{Im } S(x)} \mathcal{O}(x) / \int_{\mathbb{R}^N} dx e^{-\text{Re } S(x)}}{\int_{\mathbb{R}^N} dx e^{-\text{Re } S(x)} e^{-i\text{Im } S(x)} / \int_{\mathbb{R}^N} dx e^{-\text{Re } S(x)}} \equiv \frac{\langle e^{-i\text{Im } S(x)} \mathcal{O}(x) \rangle_{\text{rewt}}}{\langle e^{-i\text{Im } S(x)} \rangle_{\text{rewt}}}. \quad (2.2)$$

However, for systems with a large number of degrees of freedom ($N \gg 1$), both the numerator and the denominator involve highly oscillatory integrals, giving exponentially small signals of order $e^{-O(N)}$. This renders numerical evaluation via Markov chain Monte Carlo methods impractical, because the sample size N_{conf} must be exponentially large to make the statistical errors [of order $O(1/\sqrt{N_{\text{conf}}})$] relatively smaller than the signals.

In the Lefschetz thimble method, the original integration surface $\Sigma_0 = \mathbb{R}^N$ is deformed into a submanifold Σ within the complexified space \mathbb{C}^N , so that the oscillatory behavior of the integrand is alleviated on Σ (see Fig. 1). When $e^{-S(z)}$ and $e^{-S(z)}\mathcal{O}(z)$ are holomorphic over \mathbb{C}^N (which is typically the case in physical models), the value of the integral remains unchanged under the deformation that fixes the boundary, as guaranteed by Cauchy's theorem:

$$\langle \mathcal{O} \rangle = \frac{\int_{\Sigma} dz e^{-S(z)} \mathcal{O}(z)}{\int_{\Sigma} dz e^{-S(z)}}, \quad (2.3)$$

where $dz \equiv dz^1 \wedge \dots \wedge dz^N$ is the holomorphic N -form. Such a deformation can be achieved by integrating the anti-holomorphic gradient flow:

$$\dot{z} = \overline{\partial S(z)} \quad \text{with} \quad z|_{t=0} = x. \quad (2.4)$$

Here, $\dot{z} = \partial z / \partial t$, t is the deformation parameter (referred to as the flow time), and x is an

initial configuration on the original integration surface Σ_0 , with which a point on the flow is uniquely specified as $z = z(t, x)$. Due to the (in)equality

$$[S(z)]^\cdot = \partial S(z) \cdot \dot{z} = |\partial S(z)|^2 \geq 0, \quad (2.5)$$

we see that the real part $\text{Re } S(z)$ always increases under the flow except at critical points [where the gradient $\partial S(z) = (\partial_i S(z))$ vanishes] while the imaginary part $\text{Im } S(z)$ is kept constant under the flow.

As the flow time t increases, the deformed surface $\Sigma_t = \{z = z(t, x) \mid x \in \Sigma_0\}$ approaches a union of Lefschetz thimbles. Here, the Lefschetz thimble \mathcal{J} associated with a critical point ζ is defined as the set of points flowing out of ζ , on which $\text{Im } S(z)$ is constant, $\text{Im } S(z) = \text{Im } S(\zeta)$ ($z \in \mathcal{J}$) (see Fig. 1). We thus expect that the oscillatory behavior of the integrand is significantly suppressed when the flow time t becomes sufficiently large. However, the zeros of $e^{-S(z)}$ separate the deformed surface Σ , and thus Monte Carlo sampling on Σ has an ergodicity problem.² The WV-HMC method addresses this problem and is introduced as follows [13].

Since neither the numerator nor the denominator in Eq. (2.3) depends on t , we can take averages over flow time t with an arbitrary common weight $e^{-W(t)}$:

$$\langle \mathcal{O} \rangle = \frac{\int dt e^{-W(t)} \int_{\Sigma_t} dz e^{-S(z)} \mathcal{O}(z)}{\int dt e^{-W(t)} \int_{\Sigma_t} dz e^{-S(z)}}, \quad (2.6)$$

which can be viewed as a ratio of path integrals over the *worldvolume* \mathcal{R} (see Fig. 2) defined by

$$\mathcal{R} \equiv \bigcup_t \Sigma_t = \{z(t, x) \mid t \in \mathbb{R}, x \in \mathbb{R}^N\}. \quad (2.7)$$

Monte Carlo sampling over \mathcal{R} provides detours that connect regions originally separated by the potential barriers.

The extent of the worldvolume \mathcal{R} in the flow-time direction can be effectively restricted to a finite interval $[T_0, T_1]$ by adjusting the functional form of $W(t)$, which we choose as

²The interesting proposal of the *generalized thimble method* [9] is to choose a deformed integration surface at an intermediate flow time so as to alleviate both the sign problem and the ergodicity problem simultaneously. However, a detailed analysis [12] shows that, in most cases, the sign problem begins to relax only after the deformed surface touches the zeros of $e^{-S(z)}$.

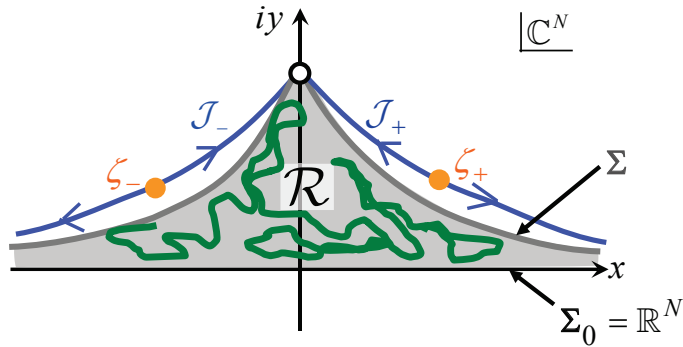


Figure 2: Worldvolume \mathcal{R} (figure adapted from Ref. [15]). ζ_{\pm} are critical points, and \mathcal{J}_{\pm} are their associated Lefschetz thimbles. The white circle stands for zeros of $e^{-S(z)}$ which behave as infinitely high potential barriers for a Monte Carlo walker.

follows (see Fig. 3) [15]:

$$W(t) = \begin{cases} -\gamma(t - T_0) + c_0 (e^{(t-T_0)^2/2d_0^2} - 1) & \text{for } t < T_0 \\ -\gamma(t - T_0) & \text{for } T_0 \leq t \leq T_1 \\ -\gamma(t - T_0) + c_1 (e^{(t-T_1)^2/2d_1^2} - 1) & \text{for } t > T_1. \end{cases} \quad (2.8)$$

Here, c_0, d_0 and c_1, d_1 determine the heights and penetration depths of the potential walls placed at $t \sim T_0$ and $t \sim T_1$, respectively. The tilt parameter γ introduces a constant driving force to prevent configurations from accumulating at small flow times. These parameters are tuned to achieve an approximately uniform distribution of configurations along flow times. The lower cutoff T_0 is chosen sufficiently small to ensure ergodicity on surfaces Σ_t at $t \sim T_0$, while the upper cutoff T_1 is taken to be sufficiently large so that the oscillatory behavior is well suppressed at $t \sim T_1$. The latter condition is verified by computing the average reweighting factor $\langle \mathcal{F}(z) \rangle_{\Sigma_t}$ at various flow times t using GT-HMC,³ which performs HMC updates on a single Σ_t [41, 42]. Configurations for measurement can be restricted further, if necessary, within a subinterval $[\tilde{T}_0, \tilde{T}_1]$, corresponding to the region $\tilde{\mathcal{R}}$ shown in Fig. 3, to exclude the lower region contaminated with the sign problem and the upper region that may be hard to sample correctly due to the complicated geometry at large flow times [13, 14].

³The HMC algorithm using the RATTLE integrator [19, 20] was first introduced to the Lefschetz thimble method in the seminal paper by the Komaba group [4], where HMC updates are performed directly on a single dominant Lefschetz thimble. Its generalization to a deformed surface $\Sigma = \Sigma_t$ at fixed t was developed in Refs. [41, 42]. The latter approach can be viewed as an HMC version of the generalized thimble method [8], and is thus referred to as the *generalized thimble Hybrid Monte Carlo* (GT-HMC) method in this paper.

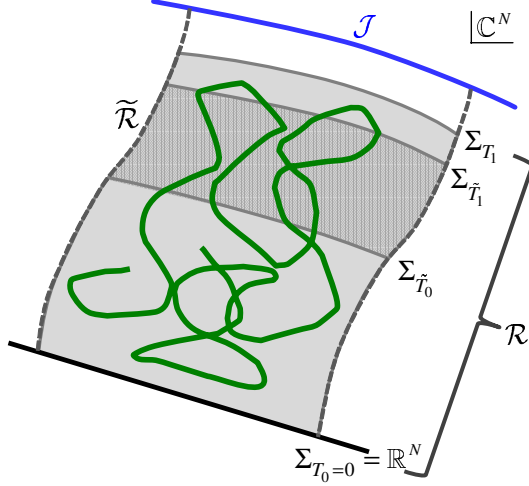


Figure 3: Worldvolume \mathcal{R} (figure adapted from Ref. [16]). Measurements can be restricted to a subregion $\tilde{\mathcal{R}}$ to improve the signal-to-noise ratio [13, 14].

The expression (2.6) can be rewritten as a ratio of reweighted averages over \mathcal{R} as [13]

$$\langle \mathcal{O} \rangle = \frac{\langle \mathcal{F}(z) \mathcal{O}(z) \rangle_{\mathcal{R}}}{\langle \mathcal{F}(z) \rangle_{\mathcal{R}}}, \quad (2.9)$$

$$\langle g(z) \rangle_{\mathcal{R}} = \frac{\int_{\mathcal{R}} |dz|_{\mathcal{R}} e^{-V(z)} g(z)}{\int_{\mathcal{R}} |dz|_{\mathcal{R}} e^{-V(z)}}. \quad (2.10)$$

Here, $V(z)$ is the potential defined by

$$V(z) = \text{Re } S(z) + W(t(z)), \quad (2.11)$$

$|dz|_{\mathcal{R}}$ is the volume element on \mathcal{R} , and $\mathcal{F}(z)$ is the associated reweighting factor,⁴

$$\mathcal{F}(z) \equiv \frac{dt dz}{|dz|_{\mathcal{R}}} e^{-i \text{Im } S(z)} = \alpha^{-1} \frac{\det E}{|\det E|} e^{-i \text{Im } S(z)}. \quad (2.12)$$

The reweighted average on \mathcal{R} [Eq. (2.10)] can be written as a phase-space integral of the form [13, 15, 16]

$$\langle g(z) \rangle_{\mathcal{R}} = \frac{\int_{T\mathcal{R}} d\Omega_{\mathcal{R}} e^{-H(z,\pi)} g(z)}{\int_{T\mathcal{R}} d\Omega_{\mathcal{R}} e^{-H(z,\pi)}}. \quad (2.13)$$

⁴ $E = (E_a^i \equiv \partial z^i / \partial x^a)$ is the Jacobian matrix. In this paper, $T_z \mathcal{S}$ ($N_z \mathcal{S}$) denotes the tangent (normal) space at z to a submanifold $\mathcal{S} \subset \mathbb{C}^N$. The flow vector $\xi \equiv \bar{\partial} S$ is decomposed into its tangential and normal components, $\xi = \xi_v + \xi_n$ ($\xi_v \in T_z \Sigma_t$, $\xi_n \in N_z \Sigma_t$), from which the lapse function α is defined as $\alpha = \sqrt{\xi_n^\dagger \xi_n}$. In GT-HMC [41, 42], the geometry in the flow-time direction is irrelevant, so that the reweighting factor does not include the factor α^{-1} and is given by a pure phase factor, $(\det E / |\det E|) e^{-i \text{Im } S} \equiv e^{i\theta}$.

Here, $\pi \in T_z\mathcal{R}$ is the momentum,⁵ and $T\mathcal{R}$ is the tangent bundle over \mathcal{R} ,

$$T\mathcal{R} = \{(z, \pi) \mid z \in \mathcal{R}, \pi \in T_z\mathcal{R}\}, \quad (2.14)$$

which carries a natural symplectic structure with symplectic form

$$\omega_{\mathcal{R}} \equiv \text{Re} \left(\overline{d\pi^i} \wedge dz^i \right). \quad (2.15)$$

The symplectic volume form $d\Omega_{\mathcal{R}}$ is given by

$$d\Omega_{\mathcal{R}} = \frac{\omega_{\mathcal{R}}^{N+1}}{(N+1)!}, \quad (2.16)$$

and the Hamiltonian $H(z, \pi)$ takes the form

$$H(z, \pi) = \frac{1}{2} \pi^\dagger \pi + V(z). \quad (2.17)$$

Molecular dynamics (MD) on $T\mathcal{R}$ (see Fig. 4) is generated by a RATTLE-type integrator [19, 20] of the following form [13] (see also Refs. [15, 16]):

$$\pi_{1/2} = \pi - \Delta s \overline{\partial V(z)} - \Delta s \lambda, \quad (2.18)$$

$$z' = z + \Delta s \pi_{1/2}, \quad (2.19)$$

$$\pi' = \pi_{1/2} - \Delta s \overline{\partial V(z')} - \Delta s \lambda'. \quad (2.20)$$

Here, Δs denotes the step size, and the force $-\overline{\partial V(z)}$ can be set to the following form [13, 15]:

$$-\overline{\partial V(z)} = -\frac{1}{2} \left[\xi + \frac{W'(t)}{\xi_n^\dagger \xi_n} \xi_n \right]. \quad (2.21)$$

The Lagrange multipliers $\lambda \in N_z\mathcal{R}$ and $\lambda' \in N_{z'}\mathcal{R}$ are determined so that $z' \in \mathcal{R}$ and $\pi' \in T_{z'}\mathcal{R}$, respectively. The former condition ($z' \in \mathcal{R}$) is equivalent to finding a triplet $\{h \in \mathbb{R}, u \in T_x\Sigma_0, \lambda \in N_z\mathcal{R}\}$ that satisfies the following relation for given $z = z(t, x) \in \mathcal{R}$ and $\pi \in T_z\mathcal{R}$:

$$z(t+h, x+u) = z + \Delta s [\pi - \Delta s \overline{\partial V(z)} - \Delta s \lambda], \quad (2.22)$$

whose solution can be obtained via simplified Newton iteration (see Ref. [15] for details). The latter condition ($\pi' \in T_{z'}\mathcal{R}$) is realized by projecting the vector $\pi_{1/2} - \Delta s \overline{\partial V(z')}$ onto the tangent space $T_{z'}\mathcal{R}$ at z' . The transformation $(z, \pi) \rightarrow (z', \pi')$ [Eqs. (2.18)–(2.20)] is exactly reversible and symplectic ($\omega'_{\mathcal{R}} = \omega_{\mathcal{R}}$), and thus volume-preserving ($d\Omega'_{\mathcal{R}} = d\Omega_{\mathcal{R}}$). Moreover,

⁵More precisely, π is the velocity.

tational cost of $O(N^3)$. The other is to employ pseudofermions and iterative solvers. This reduces the cost to $O(N^2)$, but requires careful tuning of parameters to justify the use of pseudofermions and to ensure proper convergence of the iterative solver [18]. In this paper, we focus exclusively on the first approach. A detailed discussion of the second approach will be presented in a separate publication.

3. Path-integral representation of the Hubbard model

In this section, we rewrite the grand canonical partition function of the Hubbard model in a path-integral form which is suitable for WV-HMC simulations.

3.1. The Hubbard model

The Hubbard model on a d -dimensional spatial lattice is defined by the following Hamiltonian, which includes the chemical potential term:

$$\begin{aligned} \hat{H}_\mu^{\text{org}} &= \hat{H} - \mu \hat{N} \\ &\equiv - \sum_{\mathbf{x}, \mathbf{y}} \sum_{\sigma=\uparrow, \downarrow} t_{\mathbf{xy}} c_{\mathbf{x}, \sigma}^\dagger c_{\mathbf{y}, \sigma} + U \sum_{\mathbf{x}} n_{\mathbf{x}, \uparrow} n_{\mathbf{x}, \downarrow} - \mu \sum_{\mathbf{x}} (n_{\mathbf{x}, \uparrow} + n_{\mathbf{x}, \downarrow}). \end{aligned} \quad (3.1)$$

Here, $c_{\mathbf{x}, \sigma}$ ($c_{\mathbf{x}, \sigma}^\dagger$) denotes the annihilation (creation) operator of an electron with spin σ ($=\uparrow, \downarrow$) at site $\mathbf{x} = (x_i)$ ($i = 1, \dots, d$), and $n_{\mathbf{x}, \sigma} \equiv c_{\mathbf{x}, \sigma}^\dagger c_{\mathbf{x}, \sigma}$. The hopping matrix $t_{\mathbf{xy}}$ is assumed to take the form⁶

$$t_{\mathbf{xy}} = \begin{cases} t (> 0) & \text{if } \mathbf{x} \text{ and } \mathbf{y} \text{ are nearest neighbors,} \\ 0 & \text{otherwise.} \end{cases} \quad (3.2)$$

The parameters U and μ denote the on-site interaction strength and the chemical potential, respectively. The total number operator is given by $\hat{N} = \sum_{\mathbf{x}} \sum_{\sigma} n_{\mathbf{x}, \sigma}$. We assume that the model is defined on a periodic, bipartite square lattice with linear extent L_s , so that the spatial volume is given by $V_d \equiv L_s^d$. To ensure that the bosonized action (introduced below) is manifestly real-valued at half filling, we perform a particle-hole transformation on the spin-down component as

$$a_{\mathbf{x}} \equiv c_{\mathbf{x}, \uparrow}, \quad b_{\mathbf{x}} \equiv (-1)^{\mathbf{x}} c_{\mathbf{x}, \downarrow}^\dagger, \quad (3.3)$$

⁶The same symbol t is used for both the flow time and the hopping matrix (or hopping amplitude). The intended meaning should be clear from the context.

where $(-1)^{\mathbf{x}} \equiv (-1)^{\sum_i x_i}$ is the site parity. Up to an additive constant, the Hamiltonian (3.1) is then rewritten as

$$\hat{H}_\mu \equiv \hat{H}_\mu^{\text{org}} - \mu V_d = - \sum_{\mathbf{x}, \mathbf{y}} t_{\mathbf{xy}} (a_{\mathbf{x}}^\dagger a_{\mathbf{y}} + b_{\mathbf{x}}^\dagger b_{\mathbf{y}}) + \frac{U}{2} \sum_{\mathbf{x}} (n_{\mathbf{x}}^a - n_{\mathbf{x}}^b)^2 - \tilde{\mu} \sum_{\mathbf{x}} (n_{\mathbf{x}}^a - n_{\mathbf{x}}^b), \quad (3.4)$$

where $n_{\mathbf{x}}^a \equiv a_{\mathbf{x}}^\dagger a_{\mathbf{x}}$ and $n_{\mathbf{x}}^b \equiv b_{\mathbf{x}}^\dagger b_{\mathbf{x}}$, and

$$\tilde{\mu} \equiv \mu - \frac{U}{2}. \quad (3.5)$$

Note that under the exchange of a and b , the first two terms in Eq. (3.4) remain invariant, whereas the last term changes sign. This implies that the continuum grand canonical partition function $\text{tr} e^{-\beta \hat{H}_\mu}$ is an even function of $\tilde{\mu}$. Thus, we have $\langle n_{\mathbf{x}}^a - n_{\mathbf{x}}^b \rangle = 0$ at $\tilde{\mu} = 0$, which means that the point $\tilde{\mu} = 0$ (i.e., $\mu = U/2$) corresponds to the half-filling state, $\langle n_{\mathbf{x}, \uparrow} + n_{\mathbf{x}, \downarrow} \rangle = 1$.⁷

Following Ref. [43], we introduce a redundant parameter α ($0 \leq \alpha \leq 1$) as⁸

$$(n_{\mathbf{x}}^a - n_{\mathbf{x}}^b)^2 = \alpha (n_{\mathbf{x}}^a - n_{\mathbf{x}}^b)^2 - (1 - \alpha) (n_{\mathbf{x}}^a + n_{\mathbf{x}}^b - 1)^2 + 1 - \alpha, \quad (3.6)$$

and rewrite the Hamiltonian in the form

$$\hat{H}_\mu \equiv \hat{H}_\mu^{(1)} + \hat{H}_\mu^{(2)} \quad (3.7)$$

with $\hat{H}_\mu^{(1)}$ and $\hat{H}_\mu^{(2)}$ denoting the one-body and two-body parts of the Hamiltonian, respectively:

$$\hat{H}_\mu^{(1)} \equiv - \sum_{\mathbf{x}, \mathbf{y}} (a_{\mathbf{x}}^\dagger, b_{\mathbf{x}}^\dagger) \begin{pmatrix} t_{\mathbf{xy}} + \tilde{\mu} \delta_{\mathbf{xy}} & 0 \\ 0 & t_{\mathbf{xy}} - \tilde{\mu} \delta_{\mathbf{xy}} \end{pmatrix} \begin{pmatrix} a_{\mathbf{y}} \\ b_{\mathbf{y}} \end{pmatrix} \equiv c^\dagger K c, \quad (3.8)$$

$$\hat{H}_\mu^{(2)} \equiv \frac{U}{2} \sum_{\mathbf{x}} [\alpha (n_{\mathbf{x}}^a - n_{\mathbf{x}}^b)^2 - (1 - \alpha) (n_{\mathbf{x}}^a + n_{\mathbf{x}}^b - 1)^2 + 1 - \alpha]. \quad (3.9)$$

Here, we have introduced a doublet operator c and its conjugate c^\dagger as

$$c = \begin{pmatrix} a = (a_{\mathbf{x}}) \\ b = (b_{\mathbf{x}}) \end{pmatrix}, \quad c^\dagger = (a^\dagger = (a_{\mathbf{x}}^\dagger), b^\dagger = (b_{\mathbf{x}}^\dagger)). \quad (3.10)$$

We divide the inverse temperature β into N_t time slices such that $\beta = N_t \epsilon$, and employ a

⁷This follows from $n_{\mathbf{x}, \uparrow} + n_{\mathbf{x}, \downarrow} = n_{\mathbf{x}}^a - n_{\mathbf{x}}^b + 1$.

⁸This equality directly follows from the identity $(n_{\mathbf{x}}^a + n_{\mathbf{x}}^b - 1)^2 = -(n_{\mathbf{x}}^a - n_{\mathbf{x}}^b)^2 + 1$, which holds because $(n_{\mathbf{x}}^{a/b})^2 = n_{\mathbf{x}}^{a/b}$ [43].

symmetric imaginary-time evolution operator

$$\hat{T} \equiv e^{-(\epsilon/2)\hat{H}_\mu^{(1)}} e^{-\epsilon\hat{H}_\mu^{(2)}} e^{-(\epsilon/2)\hat{H}_\mu^{(1)}}, \quad (3.11)$$

which approximates the continuum evolution operator up to second order in ϵ , $\hat{T} = e^{-\epsilon\hat{H}_\mu} + O(\epsilon^3)$. We then define the grand canonical partition function on the lattice as

$$Z \equiv \text{tr } \hat{T}^{N_t} [= \text{tr } e^{-\beta\hat{H}_\mu} + O(\epsilon^2) = e^{\beta\mu V_d} \text{tr } e^{-\beta\hat{H}_\mu^{\text{org}}} + O(\epsilon^2)]. \quad (3.12)$$

To rewrite Z in a path-integral form, we introduce a set of Grassmann variables as

$$\psi = \begin{pmatrix} \psi_a = (\psi_{a,\mathbf{x}}) \\ \psi_b = (\psi_{b,\mathbf{x}}) \end{pmatrix}, \quad \psi^\dagger = (\psi_a^\dagger = (\psi_{a,\mathbf{x}}^\dagger), \psi_b^\dagger = (\psi_{b,\mathbf{x}}^\dagger)), \quad (3.13)$$

and define the coherent state of $c = (a, b)^T$ as

$$|\psi\rangle \equiv e^{c^\dagger \psi} |0\rangle = e^{a^\dagger \psi_a + b^\dagger \psi_b} |0\rangle, \quad (3.14)$$

$$\langle\psi^\dagger| \equiv \langle 0| e^{\psi^\dagger c} = \langle 0| e^{\psi_a^\dagger a + \psi_b^\dagger b}. \quad (3.15)$$

These states satisfy the following relations:

$$\langle\psi^\dagger|\psi'\rangle = e^{\psi^\dagger \psi'}, \quad (3.16)$$

$$1 = \int d\psi^\dagger d\psi e^{-\psi^\dagger \psi} |\psi\rangle \langle\psi^\dagger|, \quad (3.17)$$

$$\text{tr } \mathcal{O} = \int d\psi^\dagger d\psi e^{-\psi^\dagger \psi} \langle\psi^\dagger| \mathcal{O} |-\psi\rangle \quad (\text{for bosonic operators } \mathcal{O}), \quad (3.18)$$

where the integration measure is defined by

$$d\psi^\dagger d\psi \equiv \prod_{\mathbf{x}} d\psi_{a,\mathbf{x}}^\dagger d\psi_{a,\mathbf{x}} \prod_{\mathbf{x}} d\psi_{b,\mathbf{x}}^\dagger d\psi_{b,\mathbf{x}}. \quad (3.19)$$

By repeatedly inserting the identity operator of the form (3.17), we obtain the Grassmann path-integral representation of Z :

$$Z = \int_{\text{ABC}} \left(\prod_{\ell=1}^{N_t} d\psi_\ell^\dagger d\psi_\ell \right) e^{-\sum_\ell \psi_\ell^\dagger \psi_\ell} \prod_{\ell=1}^{N_t} \langle\psi_\ell^\dagger| \hat{T} |\psi_{\ell-1}\rangle, \quad (3.20)$$

where ‘‘ABC’’ denotes the anti-periodic boundary condition, $\psi_0 \equiv -\psi_{N_t}$.

3.2. Bosonization

Using the identity $e^{c^\dagger X c} |\psi\rangle = |e^X \psi\rangle$ for a $(2V_d) \times (2V_d)$ matrix X acting on the doublet field, the matrix element of the transfer matrix can be written as

$$\begin{aligned} \langle \psi_\ell^\dagger | \hat{T} | \psi_{\ell-1} \rangle &= \langle \psi_\ell^\dagger | e^{-(\epsilon/2) c^\dagger K c} e^{-\epsilon \hat{H}_\mu^{(2)}} e^{-(\epsilon/2) c^\dagger K c} | \psi_{\ell-1} \rangle \\ &= \langle (e^{-(\epsilon/2) K} \psi_\ell)^\dagger | e^{-\epsilon \hat{H}_\mu^{(2)}} | e^{-(\epsilon/2) K} \psi_{\ell-1} \rangle. \end{aligned} \quad (3.21)$$

The operator $e^{-\epsilon \hat{H}_\mu^{(2)}}$ is diagonal in the site index \mathbf{x} and can be expressed as a Gaussian integral over two auxiliary (Hubbard-Stratonovich) fields [43]:

$$\begin{aligned} &e^{-(\alpha \epsilon U/2) (n_{\mathbf{x}}^a - n_{\mathbf{x}}^b)^2 + ((1-\alpha)\epsilon U/2) (n_{\mathbf{x}}^a + n_{\mathbf{x}}^b - 1)^2 - (1-\alpha)\epsilon U/2} \\ &= \int dA_{\mathbf{x}} dB_{\mathbf{x}} e^{-(1/2)(A_{\mathbf{x}}^2 + B_{\mathbf{x}}^2)} e^{[ic_0 A_{\mathbf{x}} + c_1 B_{\mathbf{x}} - c_1^2] n_{\mathbf{x}}^a} e^{[-ic_0 A_{\mathbf{x}} + c_1 B_{\mathbf{x}} - c_1^2] n_{\mathbf{x}}^b} \end{aligned} \quad (3.22)$$

with

$$c_0 \equiv \sqrt{\alpha \epsilon U}, \quad c_1 \equiv \sqrt{(1-\alpha)\epsilon U}. \quad (3.23)$$

This leads to the identity

$$\langle \psi^\dagger | e^{-\epsilon \hat{H}_\mu^{(2)}} | \psi' \rangle = \int dA dB e^{-(1/2) \sum_{\mathbf{x}} (A_{\mathbf{x}}^2 + B_{\mathbf{x}}^2)} \exp[\psi_a^\dagger e^{ic_0 A + c_1 B - c_1^2} \psi'_a + \psi_b^\dagger e^{-ic_0 A + c_1 B - c_1^2} \psi'_b], \quad (3.24)$$

where $A = (A_{\mathbf{x}} \delta_{\mathbf{x}\mathbf{y}})$, $B = (B_{\mathbf{x}} \delta_{\mathbf{x}\mathbf{y}})$, and $dA dB = \prod_{\mathbf{x}} dA_{\mathbf{x}} dB_{\mathbf{x}}$. Substituting Eqs. (3.21) and (3.24) into Eq. (3.20), the partition function becomes

$$\begin{aligned} Z &= \int \left(\prod_{\ell} dA_{\ell} dB_{\ell} \right) e^{-(1/2) \sum_{\ell, \mathbf{x}} (A_{\ell, \mathbf{x}}^2 + B_{\ell, \mathbf{x}}^2)} \int_{\text{ABC}} \left(\prod_{\ell} d\psi_{\ell}^\dagger d\psi_{\ell} \right) e^{-\sum_{\ell} \psi_{\ell}^\dagger \psi_{\ell}} \\ &\quad \times \exp \sum_{\ell} [(e^{-(\epsilon/2) K} \psi_{\ell}^\dagger)_a e^{ic_0 A_{\ell} + c_1 B_{\ell} - c_1^2} (e^{-(\epsilon/2) K} \psi_{\ell-1})_a] \\ &\quad \times \exp \sum_{\ell} [(e^{-(\epsilon/2) K} \psi_{\ell}^\dagger)_b e^{-ic_0 A_{\ell} + c_1 B_{\ell} - c_1^2} (e^{-(\epsilon/2) K} \psi_{\ell-1})_b] \\ &= \int \left(\prod_{\ell, \mathbf{x}} dA_{\ell, \mathbf{x}} dB_{\ell, \mathbf{x}} \right) e^{-(1/2) \sum_{\ell, \mathbf{x}} (A_{\ell, \mathbf{x}}^2 + B_{\ell, \mathbf{x}}^2)} \\ &\quad \times \int_{\text{ABC}} \left(\prod_{\ell, \mathbf{x}} d(\psi_a^\dagger)_{\ell, \mathbf{x}} d(\psi_a)_{\ell, \mathbf{x}} \prod_{\ell, \mathbf{x}} d(\psi_b^\dagger)_{\ell, \mathbf{x}} d(\psi_b)_{\ell, \mathbf{x}} \right) e^{-\sum_{\ell, \mathbf{x}} [(\psi_a^\dagger)_{\ell, \mathbf{x}} (\tilde{D}_a \psi_a)_{\ell, \mathbf{x}} + (\psi_b^\dagger)_{\ell, \mathbf{x}} (\tilde{D}_b \psi_b)_{\ell, \mathbf{x}}]}, \end{aligned} \quad (3.25)$$

where

$$(\tilde{D}_{a/b} \psi_{a/b})_\ell = (\psi_{a/b})_\ell - e^{(\epsilon/2)t} e^{\pm(\epsilon\tilde{\mu} + ic_0 A_\ell) + c_1 B_\ell - c_1^2} (e^{(\epsilon/2)t} \psi_{a/b})_{\ell-1}, \quad (3.26)$$

and we have rewritten $(\psi_\ell)_{a/b, \mathbf{x}}$ and $(\psi_\ell^\dagger)_{a/b, \mathbf{x}}$ as $(\psi_{a/b})_{\ell, \mathbf{x}}$ and $(\psi_{a/b}^\dagger)_{\ell, \mathbf{x}}$, respectively.

We now introduce a $(d+1)$ -dimensional spacetime lattice of volume $V_{d+1} \equiv N_t \times V_d = N_t \times L_s^d$ with coordinates denoted by $x = (\ell, \mathbf{x})$. We regard $A \equiv (A_x = A_{\ell, \mathbf{x}})$ and $B \equiv (B_x = B_{\ell, \mathbf{x}})$ as fields defined on this spacetime lattice (reusing the symbols A and B). We also define $V_{d+1} \times V_{d+1}$ matrices indexed by $x = (\ell, \mathbf{x})$ and $y = (m, \mathbf{y})$ as follows (reusing the symbol t):

$$t = (t_{xy}) \quad \text{with} \quad t_{xy} = (\delta_{\ell m} t_{\mathbf{xy}}), \quad (3.27)$$

$$\Lambda_0 = ((\Lambda_0)_{xy}) \quad \text{with} \quad (\Lambda_0)_{xy} = \begin{cases} \delta_{\ell+1, m} \delta_{\mathbf{xy}} & (\ell < N_t) \\ -\delta_{\ell, m} \delta_{\mathbf{xy}} & (\ell = N_t). \end{cases} \quad (3.28)$$

Then, the fermion operators $\tilde{D}_{a/b}$ can be written as

$$\tilde{D}_{a/b} = 1 - e^{(\epsilon/2)t} h_{a/b} \Lambda_0^{-1} e^{(\epsilon/2)t} \equiv -e^{(\epsilon/2)t} D_{a/b} \Lambda_0^{-1} e^{(\epsilon/2)t}. \quad (3.29)$$

Here, $h_{a/b} = ((h_{a/b})_x \delta_{xy})$ are diagonal matrices defined by

$$(h_{a/b})_x \equiv e^{\pm(\epsilon\tilde{\mu} + ic_0 A_x) + c_1 B_x - c_1^2}, \quad (3.30)$$

and

$$D_{a/b}(A, B) \equiv h_{a/b} - e^{-\epsilon t} \Lambda_0. \quad (3.31)$$

Finally, using the identities $\det e^{(\epsilon/2)t} = e^{(\epsilon/2) \text{tr} t} = 1$ and $\det \Lambda_0 = 1$, we arrive at the bosonized form of the partition function:

$$Z = \int dA dB e^{-S(A, B)} = \int dA dB e^{-(1/2) \sum_x (A_x^2 + B_x^2)} \det D_a(A, B) \det D_b(A, B), \quad (3.32)$$

where the measure is now defined as $dA dB \equiv \prod_x dA_x dB_x$. The partition function Z in the path-integral form remains an even function of $\tilde{\mu}$, because the change of variable $A \rightarrow -A$ renders $D_{a/b} \rightarrow D_{b/a}|_{\tilde{\mu} \rightarrow -\tilde{\mu}}$. Also, Z is real-valued, because the same transformation changes $D_{a/b} \rightarrow \overline{D_{a/b}}$.

Note that at half filling $\tilde{\mu} = 0$, we have $D_b = \overline{D_a}$, and thus $\det D_a \det D_b = |\det D_a|^2$. This implies that the path integral is free from the sign problem at half filling. Furthermore, even when $\tilde{\mu} \neq 0$, the sign problem is expected to remain mild as long as $D_b \approx \overline{D_a}$. Since the auxiliary fields A and B fluctuate around zero and c_1 , respectively, with variance of order

$O(1)$, this approximate equality is expected to hold when $\epsilon\tilde{\mu} \ll c_1 = \sqrt{(1-\alpha)\epsilon U}$, i.e., when $\alpha \ll 1 - \epsilon\tilde{\mu}^2/U$.

At $\alpha = 0$, the determinants $\det D_{a/b}$ are real on Σ_0 but can vanish. Consequently, Σ_0 becomes partitioned into disjoint regions defined by $\det D_a \det D_b \gtrless 0$. This partitioning creates ergodicity barriers on Σ_0 , rendering the WV-HMC scheme invalid. While introducing a non-zero α alleviates these ergodicity issues, excessively large values of α exacerbate the sign problem and increase the computational cost. Thus, α must be carefully tuned within a specific window: it must be large enough to ensure ergodicity on Σ_0 , yet sufficiently small to effectively suppress the sign problem [43].⁹ We perform this tuning of α in Sect. 6.

4. Applying WV-HMC to the Hubbard model

We start from the following action involving two dynamical fields A and B :

$$S(A, B) = \frac{1}{2} \sum_x (A_x^2 + B_x^2) - \ln \det D_a(A, B) - \ln \det D_b(A, B). \quad (4.1)$$

Taking into account that our evolution operator \hat{T} approximates the continuum one $e^{-\epsilon\hat{H}_\mu}$ only up to second order in ϵ , we approximate $D_{a/b}$ to the same order:¹⁰

$$D_{a/b} = h_{a/b} - \Lambda_0 + \epsilon t \Lambda_0 - \frac{\epsilon^2}{2} t^2 \Lambda_0. \quad (4.2)$$

4.1. Flow equations

Using the identities

$$\frac{\partial(h_{a/b})_y}{\partial A_x} = \pm i c_0 (h_{a/b})_x \delta_{xy}, \quad \frac{\partial(h_{a/b})_y}{\partial B_x} = c_1 (h_{a/b})_x \delta_{xy}, \quad (4.3)$$

$$\frac{\partial(D_{a/b})_{yz}}{\partial A_x} = \pm i c_0 (h_{a/b})_x \delta_{xyz}, \quad \frac{\partial(D_{a/b})_{yz}}{\partial B_x} = c_1 (h_{a/b})_x \delta_{xyz} \quad (\delta_{xyz} \equiv \delta_{xy}\delta_{yz}), \quad (4.4)$$

and defining the combinations $v_{a/b}$ from a doublet field $v = (v_x^A, v_x^B)$ as

$$(v_{a/b})_x \equiv \pm i c_0 v_x^A + c_1 v_x^B, \quad (4.5)$$

⁹Another prescription for enhancing ergodicity is to use a negative flow-time cutoff T_0 ($T_0 < 0$) [10, 13].

¹⁰Note that Λ_0 should not be estimated as $\Lambda_0 = 1 + O(\epsilon)$, because this relation holds only for thermalized configurations.

we obtain the gradient ∂S of the action and the Hessian operator H acting on a doublet field $v = (v_x^A, v_x^B)$ as follows:

$$(\partial S)_x^A \equiv \frac{\partial S}{\partial A_x} = A_x - ic_0 [(D_a^{-1})_{xx}(h_a)_x - (D_b^{-1})_{xx}(h_b)_x], \quad (4.6)$$

$$(\partial S)_x^B \equiv \frac{\partial S}{\partial B_x} = B_x - c_1 [(D_a^{-1})_{xx}(h_a)_x + (D_b^{-1})_{xx}(h_b)_x], \quad (4.7)$$

$$\begin{aligned} (Hv)_x^A &= v_x^A - ic_0 \left[(h_a)_x [(D_a^{-1})_{xx}(v_a)_x - \sum_y (D_a^{-1})_{xy}(h_a)_y(v_a)_y(D_a^{-1})_{yx}] \right. \\ &\quad \left. - (h_b)_x [(D_b^{-1})_{xx}(v_b)_x - \sum_y (D_b^{-1})_{xy}(h_b)_y(v_b)_y(D_b^{-1})_{yx}] \right], \end{aligned} \quad (4.8)$$

$$\begin{aligned} (Hv)_x^B &= v_x^B - c_1 \left[(h_a)_x [(D_a^{-1})_{xx}(v_a)_x - \sum_y (D_a^{-1})_{xy}(h_a)_y(v_a)_y(D_a^{-1})_{yx}] \right. \\ &\quad \left. + (h_b)_x [(D_b^{-1})_{xx}(v_b)_x - \sum_y (D_b^{-1})_{xy}(h_b)_y(v_b)_y(D_b^{-1})_{yx}] \right]. \end{aligned} \quad (4.9)$$

The flow equations for a configuration (A_x, B_x) , a tangent vector $v = (v_x^A, v_x^B)$, and a normal vector $n = (n_x^A, n_x^B)$ are then given by

$$\dot{A}_x = \overline{(\partial S)_x^A}, \quad \dot{B}_x = \overline{(\partial S)_x^B}, \quad (4.10)$$

$$\dot{v}_x^A = \overline{(Hv)_x^A}, \quad \dot{v}_x^B = \overline{(Hv)_x^B}, \quad (4.11)$$

$$\dot{n}_x^A = -\overline{(Hn)_x^A}, \quad \dot{n}_x^B = -\overline{(Hn)_x^B}. \quad (4.12)$$

Once the flow equations are obtained, we only need to follow the general framework presented in Sect. 2.

4.2. Observables

When the Trotter number N_t is held fixed, the parameters β and $\beta\mu$ enter the action only through ϵ and $\epsilon\tilde{\mu} = \epsilon\mu - \epsilon U/2$, respectively. We define the number density operator n and the energy density operator e as follows:¹¹

$$n(A, B) \equiv -\frac{1}{V_{d+1}} \frac{\partial S(A, B)}{\partial(\epsilon\mu)} \Big|_{\epsilon} + 1 = -\frac{1}{V_{d+1}} \frac{\partial S(A, B)}{\partial(\epsilon\tilde{\mu})} \Big|_{\epsilon} + 1, \quad (4.13)$$

$$e(A, B) \equiv \frac{\partial S(A, B)}{\partial\epsilon} \Big|_{\epsilon\mu} = \frac{1}{V_{d+1}} \left[\frac{\partial S(A, B)}{\partial\epsilon} \Big|_{\epsilon\tilde{\mu}} - \frac{U}{2} \frac{\partial S(A, B)}{\partial(\epsilon\tilde{\mu})} \Big|_{\epsilon} \right]. \quad (4.14)$$

¹¹The term $+1$ comes from the fact that the Hamiltonian (3.4) differs from the original Hamiltonian (3.1) by an additive constant $-\mu V_d$ [see Eq. (3.4)].

Their expectation values can be estimated via the path integral, and are expected to agree with the continuum expectation values of \hat{N}/V_d and \hat{H}/V_d up to $O(\epsilon^2)$ corrections:

$$\langle n \rangle \equiv \frac{1}{V_{d+1}} \frac{\int (dA dB) e^{-S(A,B)} n(A,B)}{\int (dA dB) e^{-S(A,B)}} = \frac{1}{V_d} \frac{\text{tr} e^{-\beta(\hat{H}-\mu\hat{N})} \hat{N}}{\text{tr} e^{-\beta(\hat{H}-\mu\hat{N})}} + O(\epsilon^2), \quad (4.15)$$

$$\langle e \rangle \equiv \frac{1}{V_{d+1}} \frac{\int (dA dB) e^{-S(A,B)} e(A,B)}{\int (dA dB) e^{-S(A,B)}} = \frac{1}{V_d} \frac{\text{tr} e^{-\beta(\hat{H}-\mu\hat{N})} \hat{H}}{\text{tr} e^{-\beta(\hat{H}-\mu\hat{N})}} + O(\epsilon^2). \quad (4.16)$$

Their explicit forms are given by¹²

$$n(A,B) = \frac{1}{V_{d+1}} \sum_x [(D_a^{-1})_{xx} (h_a)_x - (D_b^{-1})_{xx} (h_b)_x] + 1, \quad (4.17)$$

$$\begin{aligned} e(A,B) = \frac{1}{V_{d+1}} \sum_x & \left[\left(\frac{U}{2} - \frac{i}{2} \sqrt{\frac{\alpha U}{\epsilon}} A_x \right) [(D_a^{-1})_{xx} (h_a)_x - (D_b^{-1})_{xx} (h_b)_x] \right. \\ & + \left((1-\alpha)U - \frac{1}{2} \sqrt{\frac{(1-\alpha)U}{\epsilon}} B_x \right) [(D_a^{-1})_{xx} (h_a)_x + (D_b^{-1})_{xx} (h_b)_x] \\ & \left. - [(t D_a^{-1})_{xx} (h_a)_x + (t D_b^{-1})_{xx} (h_b)_x] \right]. \end{aligned} \quad (4.18)$$

Note that for the hopping matrix (3.2), the last line of Eq. (4.18) is written as

$$-t \sum_{i=1}^d \left\{ [(D_a^{-1})_{x+i,x} + (D_a^{-1})_{x-i,x}] (h_a)_x + [(D_b^{-1})_{x+i,x} + (D_b^{-1})_{x-i,x}] (h_b)_x \right\}, \quad (4.19)$$

where $x \pm i$ denotes a positive/negative shift of the coordinate x in the i -th direction

¹²The following formulas will be useful for derivation, which are actually exact to all orders in ϵ [$A \equiv (A_x \delta_{xy})$, $B \equiv (B_x \delta_{xy})$ and $t = (t_{xy})$]:

$$\begin{aligned} \left. \frac{\partial h_{a/b}}{\partial(\epsilon\tilde{\mu})} \right|_{\epsilon} &= \pm h_{a/b}, \\ \left. \frac{\partial h_{a/b}}{\partial\epsilon} \right|_{\epsilon\tilde{\mu}} &= h_{a/b} \left[\pm \frac{i}{2} \sqrt{\frac{\alpha U}{\epsilon}} A + \frac{1}{2} \sqrt{\frac{(1-\alpha)U}{\epsilon}} B - (1-\alpha)U \right], \\ \frac{\partial}{\partial\epsilon} \left(-e^{-\epsilon t} \Lambda_0^{-1} \right) &= h_{a/b} t - D_{a/b} t, \\ \left. \frac{\partial D_{a/b}}{\partial(\epsilon\tilde{\mu})} \right|_{\epsilon} &= \pm h_{a/b}, \\ \left. \frac{\partial D_{a/b}}{\partial\epsilon} \right|_{\epsilon\tilde{\mu}} &= h_{a/b} \left[\pm \frac{i}{2} \sqrt{\frac{\alpha U}{\epsilon}} A + \frac{1}{2} \sqrt{\frac{(1-\alpha)U}{\epsilon}} B - (1-\alpha)U + t \right] - D_{a/b} t. \end{aligned}$$

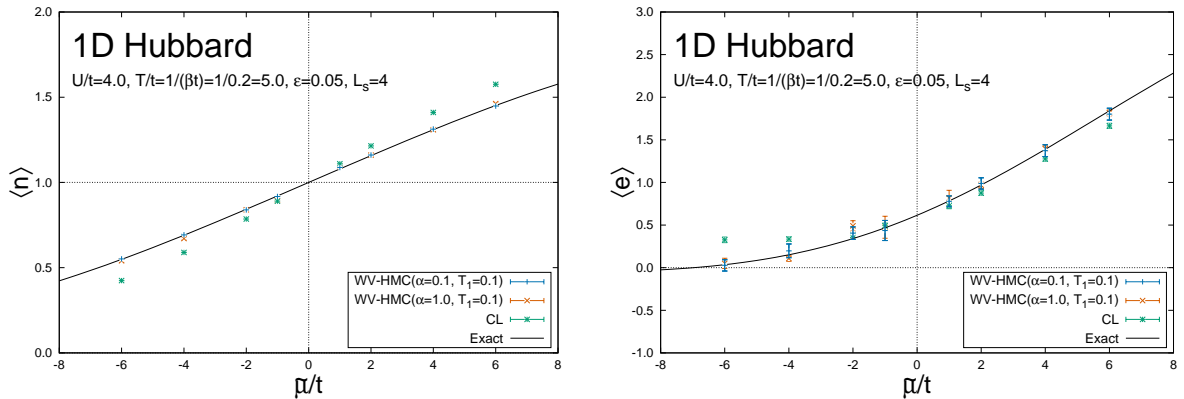


Figure 6: Number densities $\langle n \rangle$ (left) and energy densities $\langle e \rangle$ (right) obtained using WV-HMC on a spacetime lattice of size $N_t \times L_s = 4 \times 4$ (sample size: 200). The parameters are set to $t = 1.0$, $U = 4.0$, and $\beta = 0.2$, with various values of $\tilde{\mu}$. WV-HMC simulations are performed with two different values of the redundant parameter α : $\alpha = 0.1$ and $\alpha = 1.0$. Both values reproduce the exact results within statistical errors, which are smaller for smaller α (corresponding to a milder sign problem on the original integration surface Σ_0). For comparison, we also show results obtained using the complex Langevin (CL) method (sample size: 1,000), which exhibit incorrect convergence.

5. Results on the one-dimensional Hubbard model

We first verify the algorithmic correctness of WV-HMC in a simple setup with a mild sign problem. We consider a one-dimensional spatial lattice of size $L_s = 4$ at inverse temperature $\beta = 0.2$, with Trotter number $N_t = 4$ (corresponding to Trotter step $\epsilon = 0.05$). The hopping amplitude and interaction strength are set to $t = 1.0$ and $U = 4.0$, respectively. The shifted chemical potential $\tilde{\mu} = \mu - U/2$ is varied over the range $[-6.0, 6.0]$. The flow time interval is set to $[T_0, T_1] = [0.02, 0.10]$, with weight function parameters $\gamma = 0$, $c_0 = c_1 = 1$, and $d_0 = d_1 = 0.02$ [see Eq. (2.8)].

We measure the number density n [Eq. (4.17)] and the energy density e [Eq. (4.18)] using WV-HMC, with the redundant parameter α [Eq. (3.6)] set to two different values: $\alpha = 0.1$ and $\alpha = 1.0$. The exact values used for comparison are obtained using the method of Ref. [12], which is designed to yield exact results for a finite Trotter number N_t . We also compare the results with those obtained using the complex Langevin (CL) method [44, 45].

Figure 6 shows the number and energy densities obtained by the above methods. We observe that the WV-HMC results reproduce the exact values and exhibit negligible dependence on the choice of α . The figure also indicates that the CL method converges to incorrect limits, as pointed out in Ref. [46]. In fact, the histogram of the drift norm (Fig. 7) shows a long tail at large drift values, which signals the breakdown of the CL method [47] (see also Refs. [48–51]).

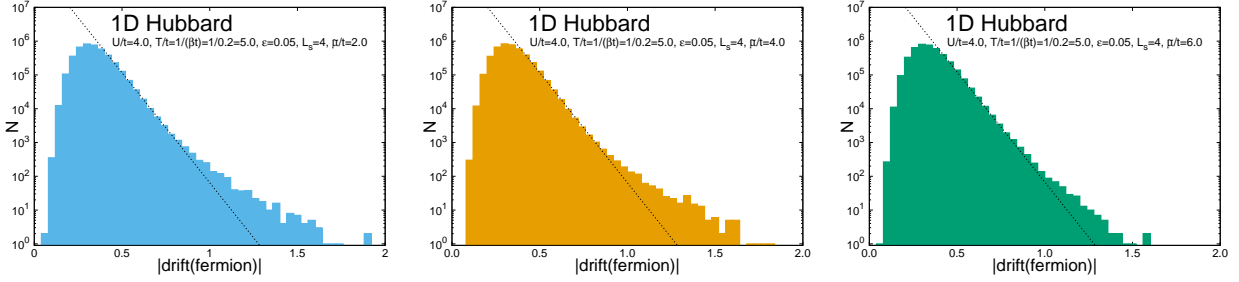


Figure 7: Histogram of the fermion drift norm in CL on a spacetime lattice of size $N_t \times L_s = 4 \times 4$. Parameters are set to $t = 1.0$, $U = 4.0$ and $\beta = 0.2$, with $\tilde{\mu} = 2.0$ (left), $\tilde{\mu} = 4.0$ (center), and $\tilde{\mu} = 6.0$ (right).

6. Results on the two-dimensional Hubbard model

We perform simulations of the two-dimensional doped Hubbard model at low temperature, including regimes where the sign problem is severe. Two spatial lattice volumes are considered: $L_s \times L_s = 6 \times 6$ and 8×8 , at inverse temperature $\beta = 6.4$ with Trotter number $N_t = 20$ (corresponding to Trotter step $\epsilon = 0.32$). The hopping amplitude and interaction strength are set to $t = 1.0$ and $U = 8.0$, respectively, corresponding to $T/t = 1/6.4 \simeq 0.156$ and $U/t = 8.0$. The shifted chemical potential $\tilde{\mu} = \mu - U/2$ is varied over the range $[0.5, 9.0]$, which includes two plateau regions in $\langle n \rangle$ at small and large values of $\tilde{\mu}$. We compare our results with those obtained using ALF [39, 40], a highly efficient non-thimble DQMC code, whose computational cost scales as $O(N_t \times V_d^3)$ when the sign problem is absent, but becomes exponential when the problem exists.

6.1. Computational cost scaling

Since we employ direct solvers for inverting the fermion matrices, the computational cost is expected to scale as $O(N^3)$, provided that the convergence rate of the Newton iteration in each RATTLE update (for solving the equation that determines the Lagrange multiplier λ) depends only weakly on the system size. Figure 8 shows the elapsed computational time per RATTLE update, clearly confirming this scaling behavior. The elapsed time is measured using GT-HMC rather than WV-HMC, because fixing the flow time yields more accurate timing measurements.

6.2. Tuning of α

To reduce the computational cost, it is desirable to suppress the sign problem on the original integration surface Σ_0 as much as possible before starting simulations. In our algorithm,

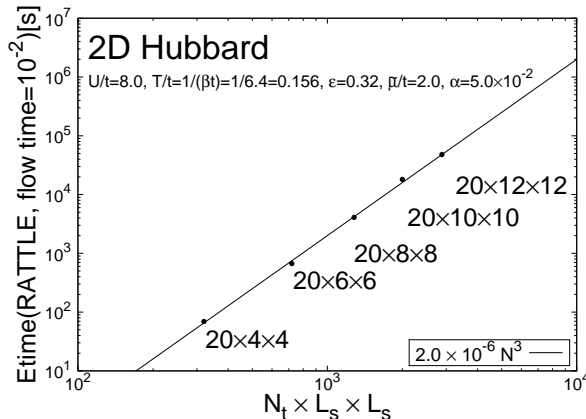


Figure 8: Elapsed time scaling of RATTLE update for various spacetime volumes.

this can be achieved by choosing a small value of α . However, care must be taken, because too small a value may lead to ergodicity issues (see Sect. 3.2) [43]. Figure 9 shows the history of the phase factor $e^{-i\text{Im}S}$ on Σ_0 for various values of α with $\tilde{\mu} = 2.0, 3.0, 4.0, 6.0$ on a spacetime lattice of volume $N_t \times L_s^2 = 20 \times 6 \times 6$. We observe that the autocorrelation time (estimated from the average plateau length) increases as α decreases. This indicates that ergodicity issues become more severe, reflecting the presence of zeros of the fermion determinants on Σ_0 . In our simulations, we adopt the following criterion for selecting α : the length of any plateau must be shorter than 10 trajectories. The selected values of α are summarized in Table 1.

$\tilde{\mu}$	0.5	1.0 – 1.8	2.0	2.2–3.0	3.5	4.0	4.5 – 9.0
α	0.5	0.1	0.05	0.01	0.008	0.006	0.005

Table 1: ($N_t \times L_s^2 = 20 \times 6 \times 6$) Tuned values of α used in WV-HMC simulations.

Figure 10 shows the histories of both the phase factor and the number density on Σ_0 obtained using the tuned values of α . The frequent fluctuations of the reweighting factor suggest that ergodicity issues are unlikely.

6.3. Sign problem after α tuning

Figure 11 shows the average phase factors on Σ_0 for a $20 \times 6 \times 6$ spacetime lattice, computed with the tuned values of α listed in Table 1. The figure demonstrates that while tuning α successfully resolves ergodicity issues on Σ_0 , it does not fully remove the sign problem. Indeed, the average phase factors are statistically consistent with zero within one standard deviation in the range $1.8 \leq \tilde{\mu} \leq 5.5$. The number densities are also shown in the same figure, exhibiting large statistical uncertainties that reflect the severity of the sign problem.

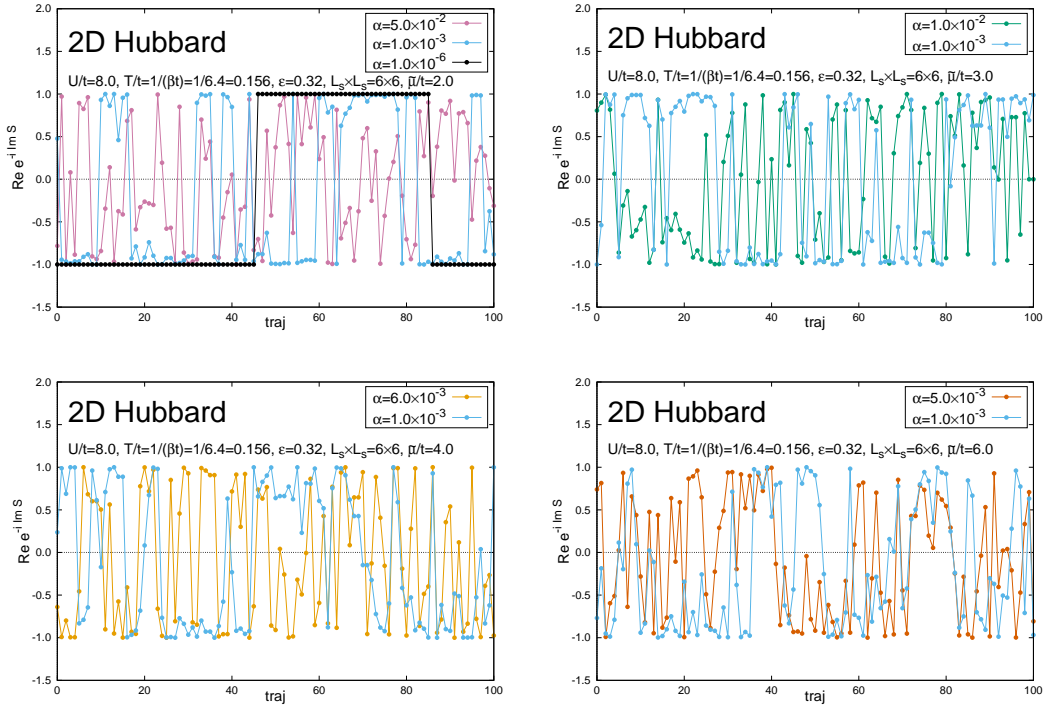


Figure 9: ($N_t \times L_s^2 = 20 \times 6 \times 6$) History of the phase factor on Σ_0 for various values of α for $\tilde{\mu} = 2.0, 3.0, 4.0, 6.0$ (from top left to bottom right).

For comparison, Fig. 12 presents results obtained using ALF on a 6×6 spatial lattice ($\epsilon = 0.01$; sample size: 50,000). These results indicate that ALF also suffers from a severe sign problem in nearly the same parameter region.¹³ Figure 13 presents results obtained using ALF on an 8×8 spatial lattice ($\epsilon = 0.01$; sample size: 50,000). We observe that the sign problem becomes more severe as the lattice volume increases.

6.4. Results on the 6×6 spatial lattice

In this subsection, we study a 6×6 spatial lattice at inverse temperature $\beta = 6.4$ with Trotter number $N_t = 20$. We also set $t = 1.0$ and $U = 8.0$. This parameter set corresponds to $T/t = 1/(t\beta) = 1/6.4 \simeq 0.156$ and $U/t = 8.0$.

Figure 14 shows the average reweighting factor on the deformed surface Σ_t at various flow times t , computed using GT-HMC, for $\tilde{\mu} = 2.0, 3.0, 4.0, 6.0$. We observe that the average becomes statistically distinguishable from zero at the two-sigma level for $t > 10^{-2}$. Based on these observations, we set the upper cutoff to $T_1 = 10^{-1}$ for the entire range of

¹³Note that the exact coincidence of the two regions is not expected, because different Hubbard-Stratonovich variables are used in ALF (Z_2 variables in ALF, while continuous Gaussian variables are used in our case).

$\tilde{\mu}$ in the WV-HMC simulations.¹⁴ The weight function parameters are chosen as $\gamma = 0$, $c_0 = c_1 = 0.01$, $d_0 = d_1 = 0.02$, with cutoffs $T_0 = 0.02$ and $T_1 = 0.10$. Figure 15 shows that the configurations efficiently explore the time interval $[T_0, T_1]$.

Figure 16 shows the average reweighting factors $\langle \mathcal{F} \rangle$ for various values of $\tilde{\mu}$. Compared with the values on Σ_0 in Fig. 11, these averages are significantly enhanced by incorporating configurations from $t > 0$ data.

Figures 17 and 18 show the number and energy densities obtained using WV-HMC. For comparison, the results obtained using ALF ($\epsilon = 0.01$; sample size: 10,000–50,000) are also included. We observe that WV-HMC yields results with small statistical uncertainties even in regions where the sign problem is severe, in sharp contrast to the results obtained using ALF.¹⁵

6.5. Results on the 8×8 spatial lattice

In this subsection, we consider an 8×8 spatial lattice at inverse temperature $\beta = 6.4$ with Trotter number $N_t = 20$. The simulation parameters are the same as those for the 6×6 case, except that we set $\gamma = 20$ to ensure nearly uniform sampling of the flow time within the interval $[T_0, T_1] = [0.02, 0.10]$.¹⁶ Figure 19 confirms that the entire region of flow time is sampled. Figure 20 shows that the average reweighting factors are statistically nonvanishing at the one-sigma level.

Figures 21 and 22 present the number and energy densities obtained using WV-HMC. We also include the results obtained using ALF for comparison ($\epsilon = 0.01$; sample size: 10,000–50,000). Although the number of configurations is currently limited, the WV-HMC results remain statistically robust across the entire parameter range, as in the 6×6 case.

¹⁴The value $T_1 = 10^{-1}$ is in fact too large for significantly reducing the sign problem. However, choosing a smaller value restricts the worldvolume to a thin layer, for which configurations cannot be explored efficiently, reintroducing ergodicity issues into the WV-HMC simulations. A prescription for enhancing ergodicity in such a thin worldvolume is to embed GT-HMC in WV-HMC, as discussed in detail in Ref. [38].

¹⁵A discrepancy in $\langle e \rangle$ between WV-HMC and ALF is observed in the parameter region free from the sign problem. We confirm that this discrepancy originates from the finite Trotter step and vanishes in the continuum limit $\epsilon \rightarrow 0$ [38].

¹⁶A positive value of γ is required for large lattices; otherwise, the MD force [which acts in the direction opposite to the flow; see Eq. (2.21)] causes configurations to accumulate near the bottom of the worldvolume (see Refs. [13, 15] for detailed explanations). One can neglect this effect and set $\gamma = 0$ for small lattices because the momentum refresh at the beginning of each MD trajectory spreads configurations isotropically throughout the worldvolume.

7. Conclusions and outlook

In this paper, we applied the Worldvolume Hybrid Monte Carlo (WV-HMC) algorithm [13] to the two-dimensional doped Hubbard model. We used direct solvers for the inversion of fermion matrices and confirmed that the computational cost scales as $O(N^3)$, in agreement with theoretical expectations. We evaluated the number density $\langle n \rangle$ and the energy density $\langle e \rangle$ on 6×6 and 8×8 lattices at $T/t = 1/(t\beta) = 1/6.4 \simeq 0.156$ and $U/t = 8.0$ with Trotter number $N_t = 20$, and demonstrated that the WV-HMC method remains efficient, with well-controlled statistical errors even in parameter regions where the standard DQMC methods fail due to severe sign problems.

Although the computational cost of $O(N^3)$ remains high for practical calculations, especially when approaching the thermodynamic limit, our results suggest that the WV-HMC framework can serve as a powerful tool for investigating the doped Hubbard model. In fact, the cost can be reduced to $O(N^2)$ by introducing pseudofermions and employing iterative solvers [18]. However, this approach requires careful parameter tuning, a detailed study of which will be presented in a separate publication.

Even at finite spatial volumes, it is important to take the continuum limit in the temporal direction ($\epsilon \rightarrow 0$), because the Trotter step ϵ used in the present paper is still relatively large ($\epsilon = 0.32$), although the code is designed such that finite-size corrections in the observables are $O(\epsilon^2)$. In the subsequent paper [38], we take the continuum limit after developing a method that enables us to reduce the maximum flow time while avoiding ergodicity issues in such a thin worldvolume.

To investigate the model in the ground-state regime, one must further extrapolate to the $\beta \rightarrow \infty$ limit, using sufficiently large values of β that already realize the $\epsilon \rightarrow 0$ limit. It would then be highly interesting to compare the zero-temperature Monte Carlo results (obtained using WV-HMC) with those from other approaches, such as variational Monte Carlo, constrained-path auxiliary-field quantum Monte Carlo, and density functional theory. One of the most informative indicators for such a comparison, which we plan to adopt, is the *V-score* [52], a benchmark based on the variance of the ground-state energy.¹⁷

In parallel with the present study, we are extending the WV-HMC method to other systems. An extension to group manifolds has already been completed [16]. Current targets include finite-density QCD, other strongly correlated electron systems, and real-time dynamics of quantum many-body systems. Results from these ongoing efforts will be reported in future publications.

¹⁷We thank Masatoshi Imada for suggesting this comparison scheme.

Acknowledgments

The authors thank Sinya Aoki, Fakher F. Assaad, Masatoshi Imada, Ken-Ichi Ishikawa, Issaku Kanamori, Yoshio Kikukawa, Nobuyuki Matsumoto, Yusuke Nomura, Maksim Ulybyshev, Youhei Yamaji, and Shiwei Zhang for valuable discussions. M.F. acknowledges that parts of the basic lattice-field infrastructure of the code were developed using the FermiQCD/MDP library [53]. The WV-HMC algorithmic components, together with the configuration generation, random-number generation, fermion-matrix construction and solvers, and routines for observable measurements, were implemented independently by M.F. This work was partially supported by JSPS KAKENHI (Grant Numbers JP20H01900, JP21K03553, JP23H00112, JP23H04506, JP24K07052, JP25H01533); by MEXT as “Program for Promoting Researches on the Supercomputer Fugaku” (Simulation for basic science: approaching the new quantum era, JPMXP1020230411); and by SPIRIT2 2025 of Kyoto University.

References

- [1] E. Witten, “Analytic continuation of Chern-Simons theory,” *AMS/IP Stud. Adv. Math.* **50**, 347-446 (2011) [arXiv:1001.2933 [hep-th]].
- [2] M. Cristoforetti, F. Di Renzo and L. Scorzato, “New approach to the sign problem in quantum field theories: High density QCD on a Lefschetz thimble,” *Phys. Rev. D* **86**, 074506 (2012) [arXiv:1205.3996 [hep-lat]].
- [3] M. Cristoforetti, F. Di Renzo, A. Mukherjee and L. Scorzato, “Monte Carlo simulations on the Lefschetz thimble: Taming the sign problem,” *Phys. Rev. D* **88**, no. 5, 051501(R) (2013) [arXiv:1303.7204 [hep-lat]].
- [4] H. Fujii, D. Honda, M. Kato, Y. Kikukawa, S. Komatsu and T. Sano, “Hybrid Monte Carlo on Lefschetz thimbles - A study of the residual sign problem,” *JHEP* **1310**, 147 (2013) [arXiv:1309.4371 [hep-lat]].
- [5] H. Fujii, S. Kamata and Y. Kikukawa, “Lefschetz thimble structure in one-dimensional lattice Thirring model at finite density,” *JHEP* **11**, 078 (2015) [erratum: *JHEP* **02**, 036 (2016)] [arXiv:1509.08176 [hep-lat]].
- [6] H. Fujii, S. Kamata and Y. Kikukawa, “Monte Carlo study of Lefschetz thimble structure in one-dimensional Thirring model at finite density,” *JHEP* **12**, 125 (2015) [erratum: *JHEP* **09**, 172 (2016)] [arXiv:1509.09141 [hep-lat]].
- [7] A. Alexandru, G. Başar and P. Bedaque, “Monte Carlo algorithm for simulating fermions on Lefschetz thimbles,” *Phys. Rev. D* **93**, no. 1, 014504 (2016) [arXiv:1510.03258 [hep-lat]].

- [8] A. Alexandru, G. Başar, P. F. Bedaque, G. W. Ridgway and N. C. Warrington, “Sign problem and Monte Carlo calculations beyond Lefschetz thimbles,” *JHEP* **1605**, 053 (2016) [arXiv:1512.08764 [hep-lat]].
- [9] A. Alexandru, G. Basar, P. F. Bedaque and G. W. Ridgway, “Schwinger-Keldysh formalism on the lattice: A faster algorithm and its application to field theory,” *Phys. Rev. D* **95**, no.11, 114501 (2017) [arXiv:1704.06404 [hep-lat]].
- [10] M. Fukuma and N. Umeda, “Parallel tempering algorithm for integration over Lefschetz thimbles,” *PTEP* **2017**, no. 7, 073B01 (2017) [arXiv:1703.00861 [hep-lat]].
- [11] A. Alexandru, G. Başar, P. F. Bedaque and N. C. Warrington, “Tempered transitions between thimbles,” *Phys. Rev. D* **96**, no. 3, 034513 (2017) [arXiv:1703.02414 [hep-lat]].
- [12] M. Fukuma, N. Matsumoto and N. Umeda, “Applying the tempered Lefschetz thimble method to the Hubbard model away from half-filling,” *Phys. Rev. D* **100**, no.11, 114510 (2019) [arXiv:1906.04243 [cond-mat.str-el]].
- [13] M. Fukuma and N. Matsumoto, “Worldvolume approach to the tempered Lefschetz thimble method,” *PTEP* **2021**, no.2, 023B08 (2021) [arXiv:2012.08468 [hep-lat]].
- [14] M. Fukuma, N. Matsumoto and Y. Namekawa, “Statistical analysis method for the worldvolume hybrid Monte Carlo algorithm,” *PTEP* **2021**, no.12, 123B02 (2021) [arXiv:2107.06858 [hep-lat]].
- [15] M. Fukuma, “Simplified Algorithm for the Worldvolume HMC and the generalized thimble HMC,” *PTEP* **2024**, no.5, 053B02 (2024) [arXiv:2311.10663 [hep-lat]].
- [16] M. Fukuma, “Worldvolume Hybrid Monte Carlo algorithm for group manifolds,” [arXiv:2506.12002 [hep-lat]].
- [17] M. Fukuma and Y. Namekawa, “Applying the Worldvolume Hybrid Monte Carlo method to the finite-density complex ϕ^4 model and the Hubbard model,” *PoS LATTICE2023*, 178 (2024)
- [18] M. Fukuma and Y. Namekawa, “Applying the Worldvolume Hybrid Monte Carlo method to the two-dimensional Hubbard model,” *PoS LATTICE2024*, 053 (2025)
- [19] H. C. Andersen, “RATTLE: A “velocity” version of the SHAKE algorithm for molecular dynamics calculations,” *J. Comput. Phys.* **52**, 24 (1983).
- [20] B. J. Leimkuhler and R. D. Skeel, “Symplectic numerical integrators in constrained Hamiltonian systems,” *J. Comput. Phys.* **112**, 117 (1994).
- [21] H. Yokoyama and H. Shiba, “Variational Monte-Carlo Studies of Hubbard Model. I,” *J. Phys. Soc. Jpn.* **56**, 1490 (1987).

- [22] S. Sorella, “Wave function optimization in the variational Monte Carlo method,” *Phys. Rev. B* **71**, 241103 (2005) [arXiv:cond-mat/0502553].
- [23] K. Yamaji, *et al.*, “Variational Monte Carlo study on the superconductivity in the two-dimensional Hubbard model,” *Physica C: Superconductivity* **304** 225 (1998) [arXiv:cond-mat/9806210].
- [24] D. Tahara and M. Imada, “Variational Monte Carlo method combined with quantum-number projection and multi-variable optimization.” *J. Phys. Soc. Jpn.* **77** 114701 (2008) [arXiv:0805.4457].
- [25] S. Zhang, J. Carlson and J. E. Gubernatis, “Constrained Path Quantum Monte Carlo Method for Fermion Ground States,” *Phys. Rev. Lett.* **74**, 3652-3655 (1995) [arXiv:cond-mat/9503055 [cond-mat]].
- [26] S. Zhang, J. Carlson and J. E. Gubernatis, “Constrained path Monte Carlo method for fermion ground states,” *Phys. Rev. B* **55**, 7464 (1997) [arXiv:cond-mat/9607062].
- [27] A. Mukherjee and M. Cristoforetti, “Lefschetz thimble Monte Carlo for many-body theories: A Hubbard model study,” *Phys. Rev. B* **90**, no.3, 035134 (2014) [arXiv:1403.5680 [cond-mat.str-el]].
- [28] M. V. Ulybyshev and S. N. Valgushev, “Path integral representation for the Hubbard model with reduced number of Lefschetz thimbles,” [arXiv:1712.02188 [cond-mat.str-el]].
- [29] M. Ulybyshev, C. Winterowd and S. Zafeiropoulos, “Taming the sign problem of the finite density Hubbard model via Lefschetz thimbles,” [arXiv:1906.02726 [cond-mat.str-el]].
- [30] M. Ulybyshev, C. Winterowd and S. Zafeiropoulos, “Lefschetz thimbles decomposition for the Hubbard model on the hexagonal lattice,” *Phys. Rev. D* **101**, no.1, 014508 (2020) [arXiv:1906.07678 [cond-mat.str-el]].
- [31] M. Ulybyshev, C. Winterowd, F. Assaad and S. Zafeiropoulos, “Instanton gas approach to the Hubbard model,” *Phys. Rev. B* **107**, no.4, 045143 (2023) [arXiv:2207.06297 [cond-mat.str-el]].
- [32] M. Ulybyshev and F. F. Assaad, “Beyond the instanton gas approach: dominant thimbles approximation for the Hubbard model,” [arXiv:2407.09452 [cond-mat.str-el]].
- [33] S. Akiyama and Y. Kuramashi, “Tensor renormalization group approach to (1+1)-dimensional Hubbard model,” *Phys. Rev. D* **104**, no.1, 014504 (2021) [arXiv:2105.00372 [hep-lat]].
- [34] S. Akiyama, Y. Kuramashi and T. Yamashita, “Metal–insulator transition in the (2+1)-dimensional Hubbard model with the tensor renormalization group,” *PTEP* **2022**, no.2, 023I01 (2022) [arXiv:2109.14149 [cond-mat.str-el]].

- [35] M. Rodekamp, E. Berkowitz, C. Gäntgen, S. Krieg, T. Luu and J. Ostmeyer, “Mitigating the Hubbard sign problem with complex-valued neural networks,” *Phys. Rev. B* **106**, no.12, 125139 (2022) [arXiv:2203.00390 [physics.comp-ph]].
- [36] C. Gäntgen, E. Berkowitz, T. Luu, J. Ostmeyer and M. Rodekamp, “Fermionic sign problem minimization by constant path integral contour shifts,” *Phys. Rev. B* **109**, no.19, 195158 (2024) [arXiv:2307.06785 [cond-mat.str-el]].
- [37] D. Schuh, J. Kreit, E. Berkowitz, L. Funcke, T. Luu, K. A. Nicoli and M. Rodekamp, “Simulating the Hubbard Model with Equivariant Normalizing Flows,” *PoS LATTICE2024*, 069 (2025) [arXiv:2501.07371 [cond-mat.str-el]].
- [38] M. Fukuma and Y. Namekawa, “Enhancing the ergodicity of Worldvolume HMC via embedding generalized thimble HMC,” [arXiv:2508.02659 [cond-mat.str-el]].
- [39] M. Bercx, F. Goth, J. S. Hofmann and F. F. Assaad, “The ALF (Algorithms for Lattice Fermions) project release 1.0. Documentation for the auxiliary field quantum Monte Carlo code,” *SciPost Phys.* **3**, no.2, 013 (2017) [arXiv:1704.00131 [cond-mat.str-el]].
- [40] F. F. Assaad *et al.* [ALF], “The ALF (Algorithms for Lattice Fermions) project release 2.4. Documentation for the auxiliary-field quantum Monte Carlo code,” *SciPost Phys. Codeb.* **2022**, 1 (2022) [arXiv:2012.11914 [cond-mat.str-el]].
- [41] A. Alexandru, “Improved algorithms for generalized thimble method,” talk at the 37th international conference on lattice field theory, Wuhan, 2019.
- [42] M. Fukuma, N. Matsumoto and N. Umeda, “Implementation of the HMC algorithm on the tempered Lefschetz thimble method,” [arXiv:1912.13303 [hep-lat]].
- [43] S. Beyl, F. Goth and F. F. Assaad, “Revisiting the Hybrid Quantum Monte Carlo Method for Hubbard and Electron-Phonon Models,” *Phys. Rev. B* **97**, no.8, 085144 (2018) [arXiv:1708.03661 [cond-mat.str-el]].
- [44] G. Parisi, “On complex probabilities,” *Phys. Lett. B* **131**, 393 (1983).
- [45] J.R. Klauder, “Coherent State Langevin Equations for Canonical Quantum Systems With Applications to the Quantized Hall Effect,” *Phys. Rev. A* **29**, 2036 (1984).
- [46] A. Yamamoto and T. Hayata, “Complex Langevin simulation in condensed matter physics,” *PoS LATTICE2015*, 041 (2016) [arXiv:1508.00415 [hep-lat]].
- [47] K. Nagata, J. Nishimura and S. Shimasaki, “Argument for justification of the complex Langevin method and the condition for correct convergence,” *Phys. Rev. D* **94**, no.11, 114515 (2016) [arXiv:1606.07627 [hep-lat]].
- [48] G. Aarts, E. Seiler and I. O. Stamatescu, “The Complex Langevin method: When can it be trusted?,” *Phys. Rev. D* **81**, 054508 (2010) [arXiv:0912.3360 [hep-lat]].

- [49] G. Aarts, F. A. James, E. Seiler and I. O. Stamatescu, “Complex Langevin: Etiology and Diagnostics of its Main Problem,” *Eur. Phys. J. C* **71**, 1756 (2011) [arXiv:1101.3270 [hep-lat]].
- [50] J. Nishimura and S. Shimasaki, “New Insights into the Problem with a Singular Drift Term in the Complex Langevin Method,” *Phys. Rev. D* **92**, no.1, 011501 (2015) [arXiv:1504.08359 [hep-lat]].
- [51] K. Nagata, J. Nishimura and S. Shimasaki, “Justification of the complex Langevin method with the gauge cooling procedure,” *PTEP* **2016**, no.1, 013B01 (2016) [arXiv:1508.02377 [hep-lat]].
- [52] D. Wu, R. Rossi, F. Vicentini, N. Astrakhantsev, F. Becca, X. Cao, J. Carrasquilla, F. Ferrari, A. Georges, M. Hibat-Allah and M. Imada, *et al.* “Variational benchmarks for quantum many-body problems,” *Science* **386**, no.6719, adg9774 (2024) [arXiv:2302.04919 [quant-ph]].
- [53] M. Di Pierro, “FermiQCD: A Tool Kit for Parallel Lattice QCD Applications,” *Nucl. Phys. B Proc. Suppl.* **106**, 1034-1036 (2002) [arXiv:hep-lat/0110116 [hep-lat]].

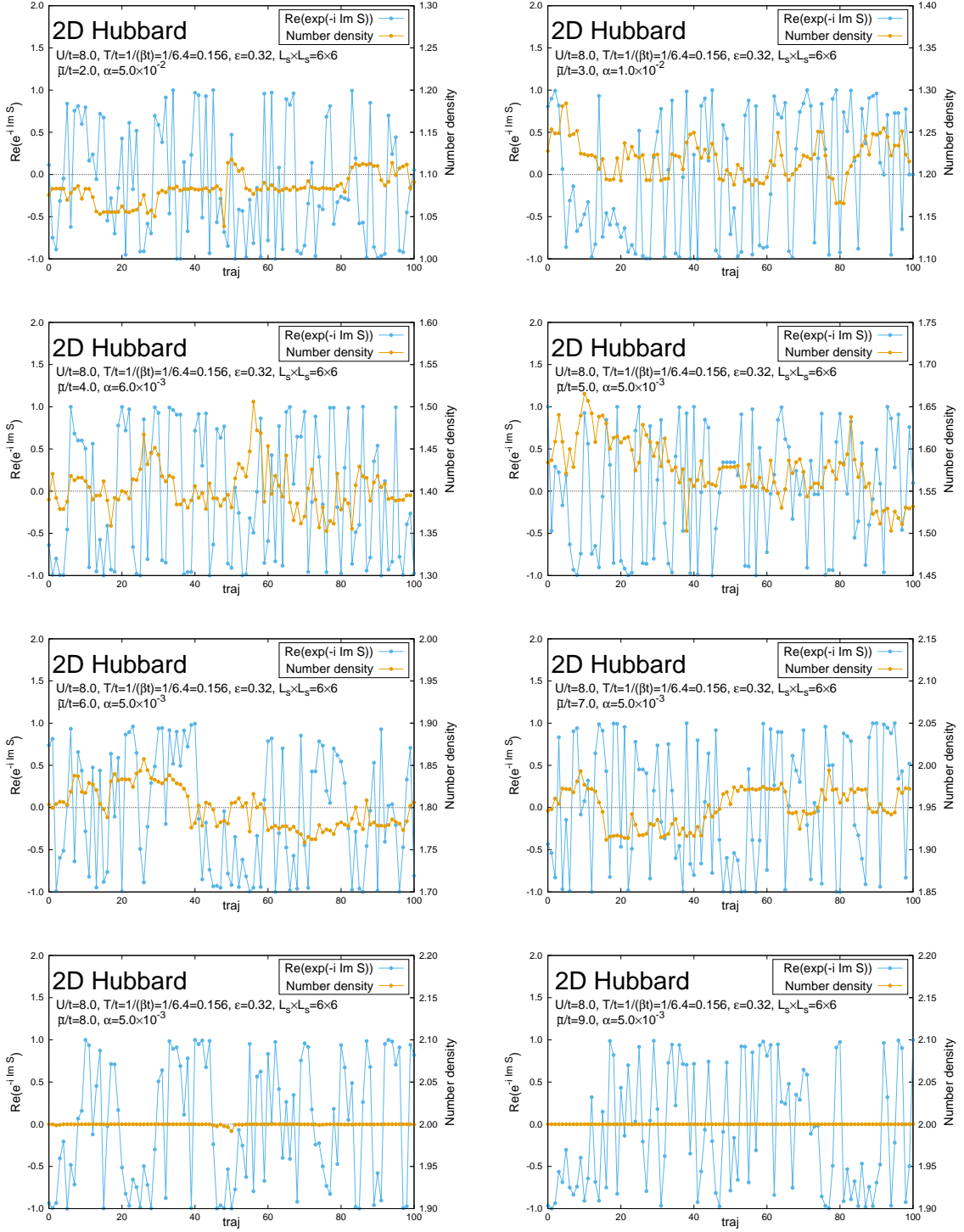


Figure 10: ($N_t \times L_s^2 = 20 \times 6 \times 6$) Histories of the phase factor and the number density on Σ_0 obtained using the tuned values of α in Table 1. $\tilde{\mu}$ is varied from 2.0 to 9.0 (from top left to bottom right).

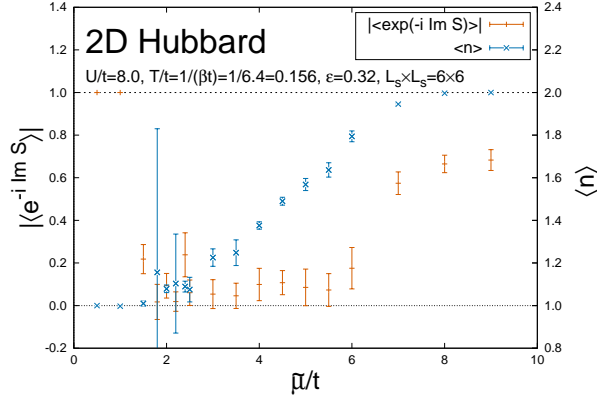


Figure 11: ($N_t \times L_s^2 = 20 \times 6 \times 6$) Average phase factors and number densities on Σ_0 at various values of $\tilde{\mu}$.

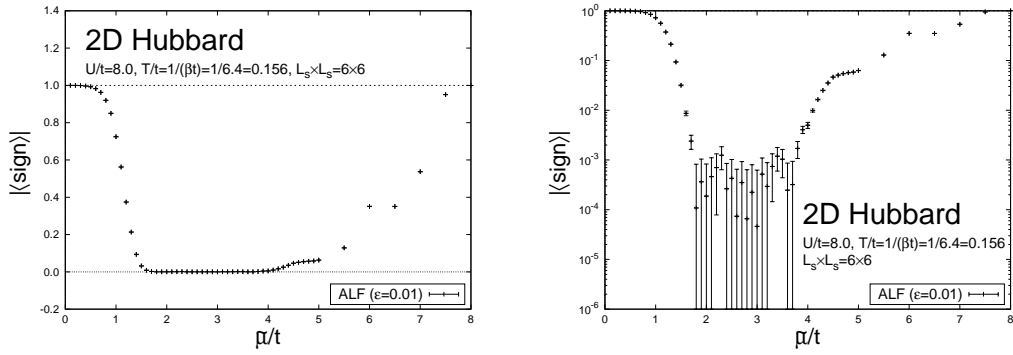


Figure 12: ($N_t \times L_s^2 = 20 \times 6 \times 6$) Average signs at various values of $\tilde{\mu}$ obtained using ALF.

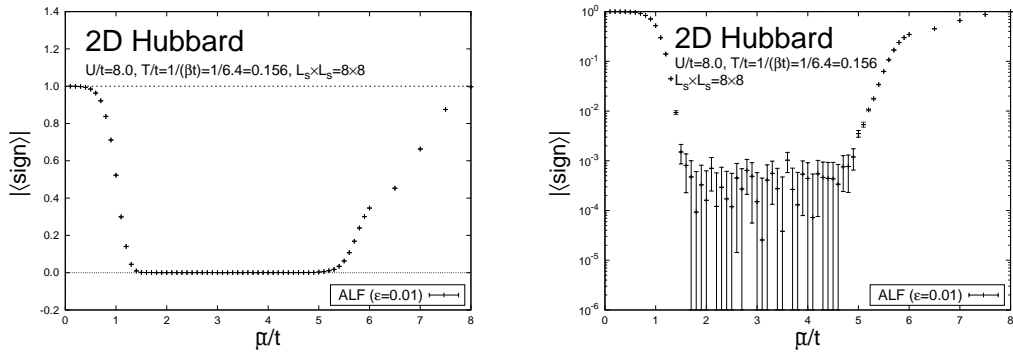


Figure 13: ($N_t \times L_s^2 = 20 \times 8 \times 8$) Average signs at various values of $\tilde{\mu}$ obtained using ALF.

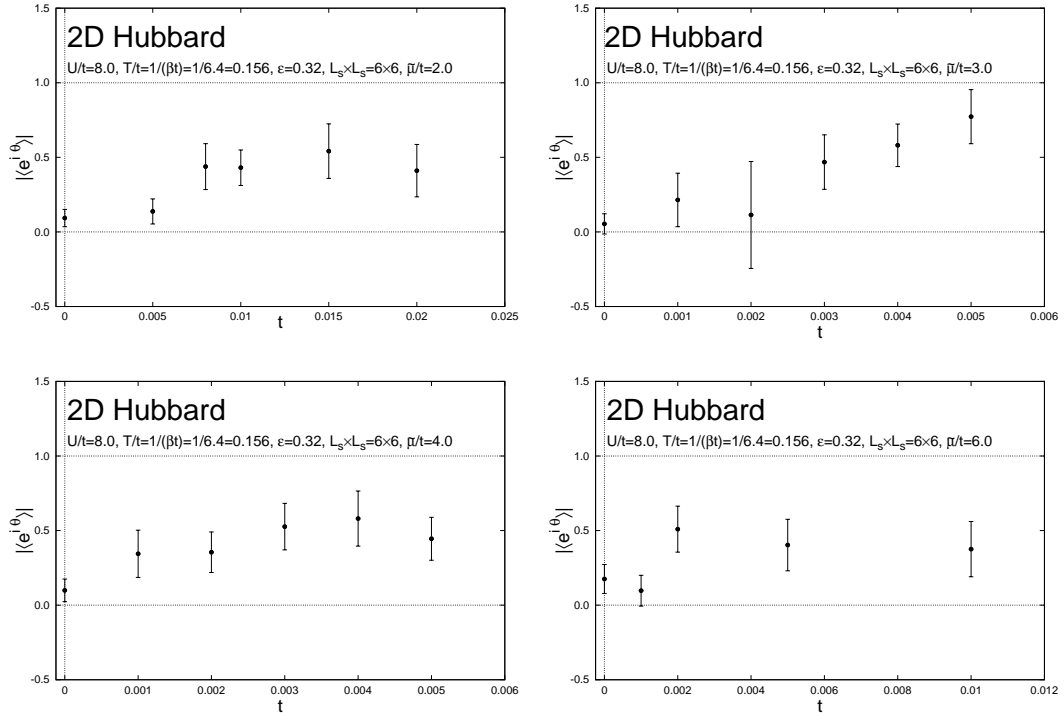


Figure 14: ($N_t \times L_s^2 = 20 \times 6 \times 6$) Flow-time dependence of the average reweighting factor $\langle e^{i\theta} \rangle$ for various values of $\tilde{\mu}$, obtained using GT-HMC [$e^{i\theta} \equiv (\det E / |\det E|) e^{-i \text{Im} S}$].

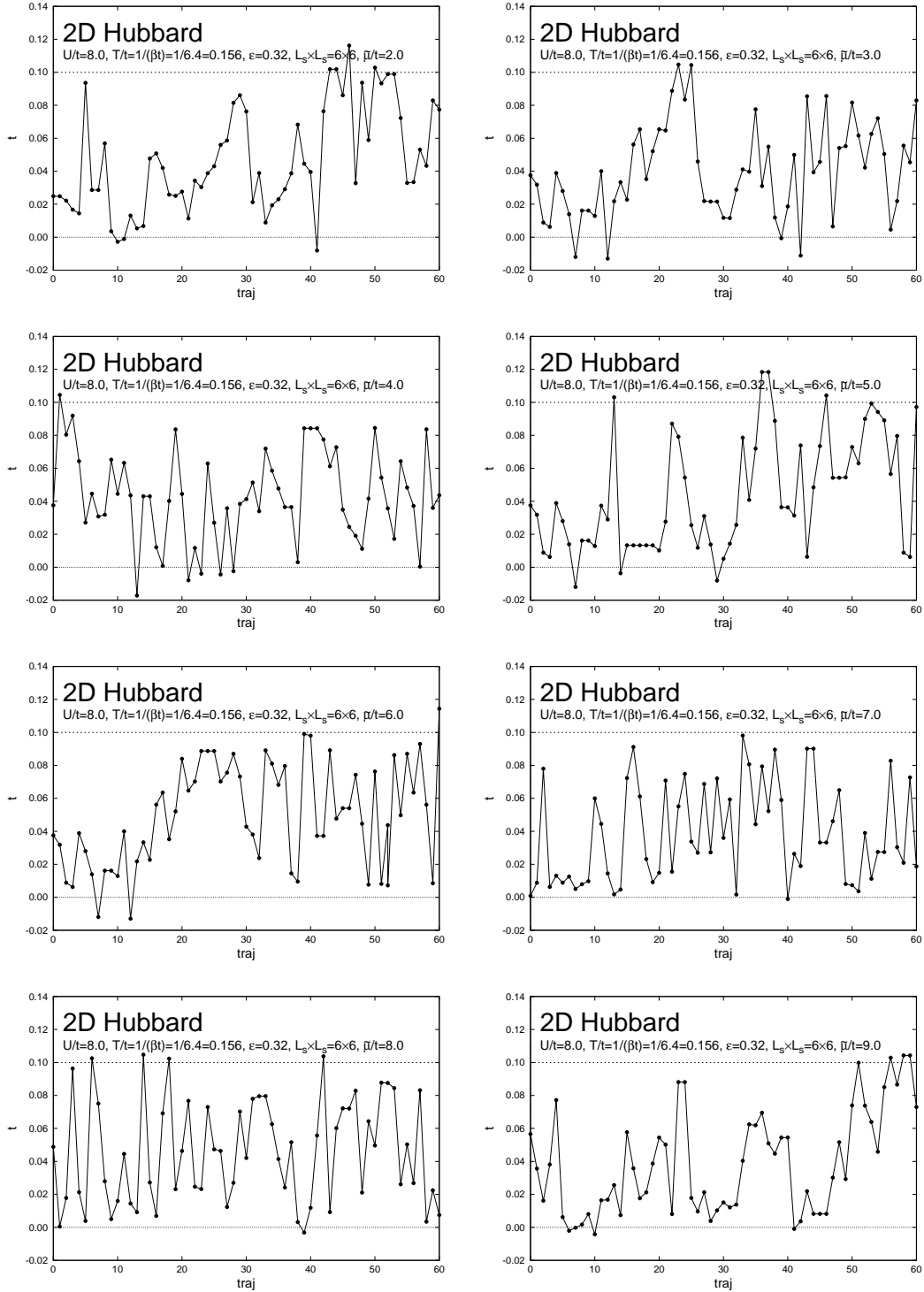


Figure 15: ($N_t \times L_s^2 = 20 \times 6 \times 6$) History of the flow time in WV-HMC.

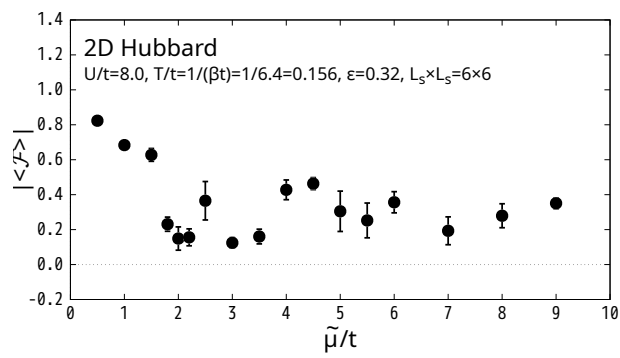


Figure 16: ($N_t \times L_s^2 = 20 \times 6 \times 6$) Average reweighting factors obtained using WV-HMC.

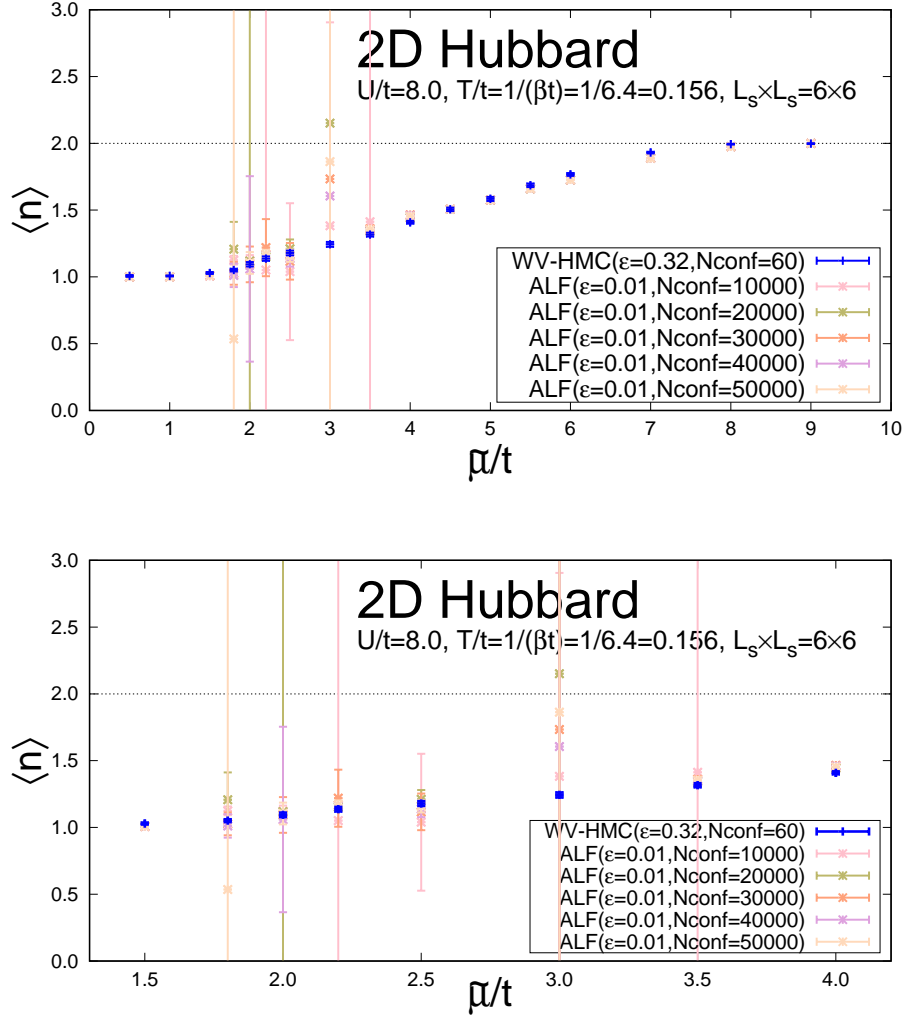


Figure 17: ($N_t \times L_s^2 = 20 \times 6 \times 6$) Number densities obtained using WV-HMC. ALF results are shown for comparison. Top: Full range of $\tilde{\mu}$. Bottom: Enlarged view of $1.5 \leq \tilde{\mu} \leq 4.0$, including ALF results with five different sample sizes.

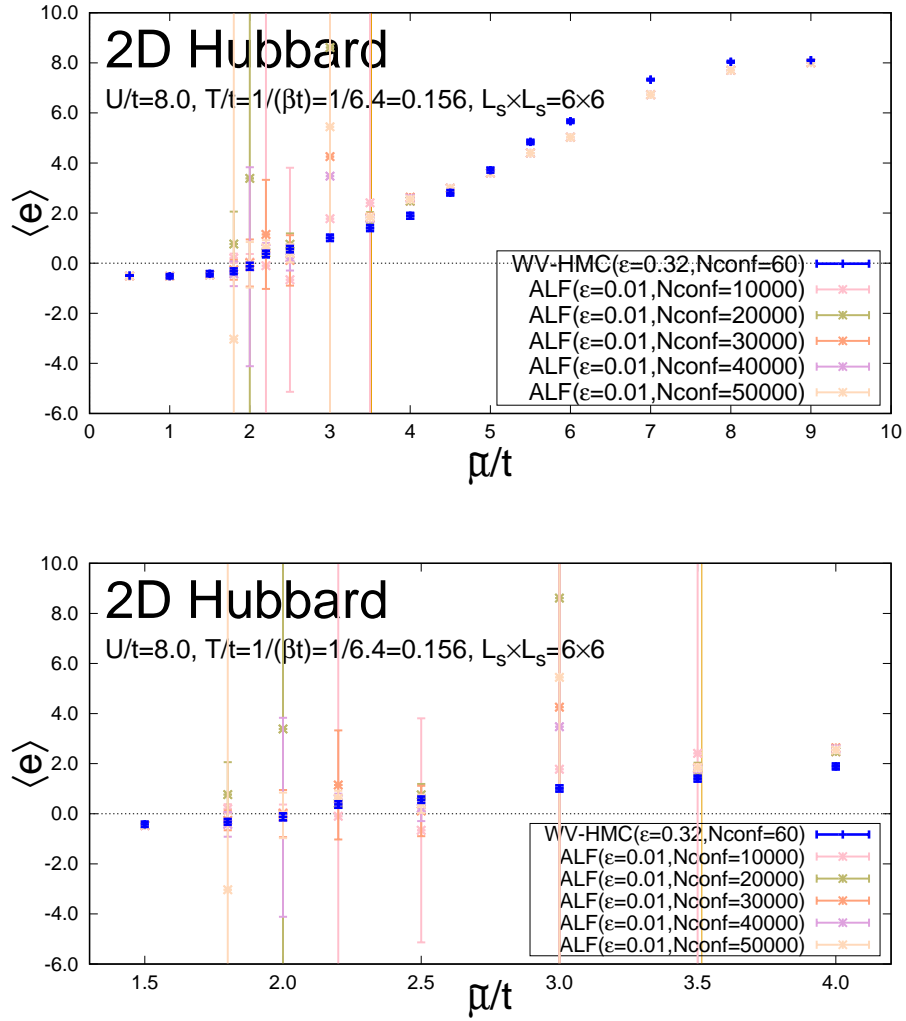


Figure 18: ($N_t \times L_s^2 = 20 \times 6 \times 6$) Energy densities obtained using WV-HMC. ALF results are shown for comparison. Top: Full range of $\tilde{\mu}$. Bottom: Enlarged view of $1.5 \leq \tilde{\mu} \leq 4.0$, including ALF results with five different sample sizes.

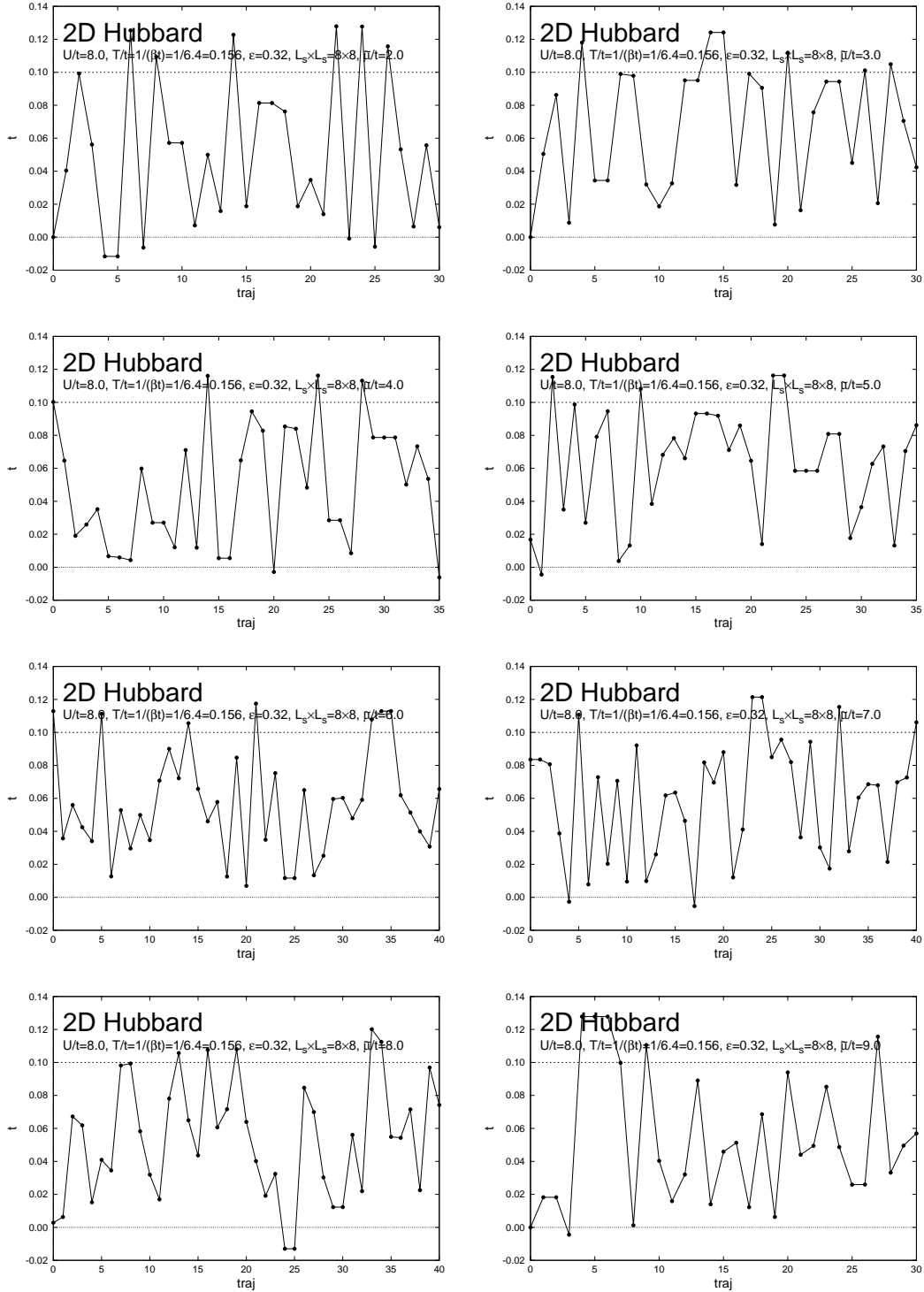


Figure 19: $(N_t \times L_s^2 = 20 \times 8 \times 8)$ History of the flow time in WV-HMC.

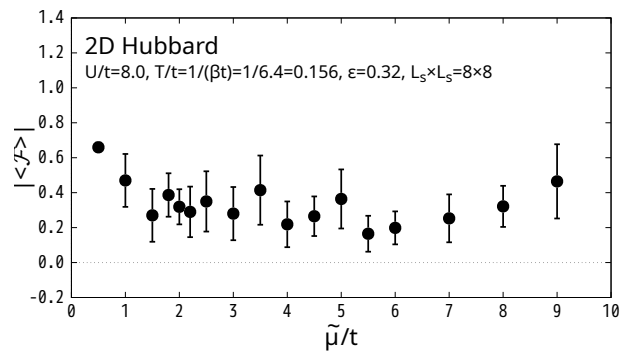


Figure 20: ($N_t \times L_s^2 = 20 \times 8 \times 8$) Average reweighting factors obtained using WV-HMC.

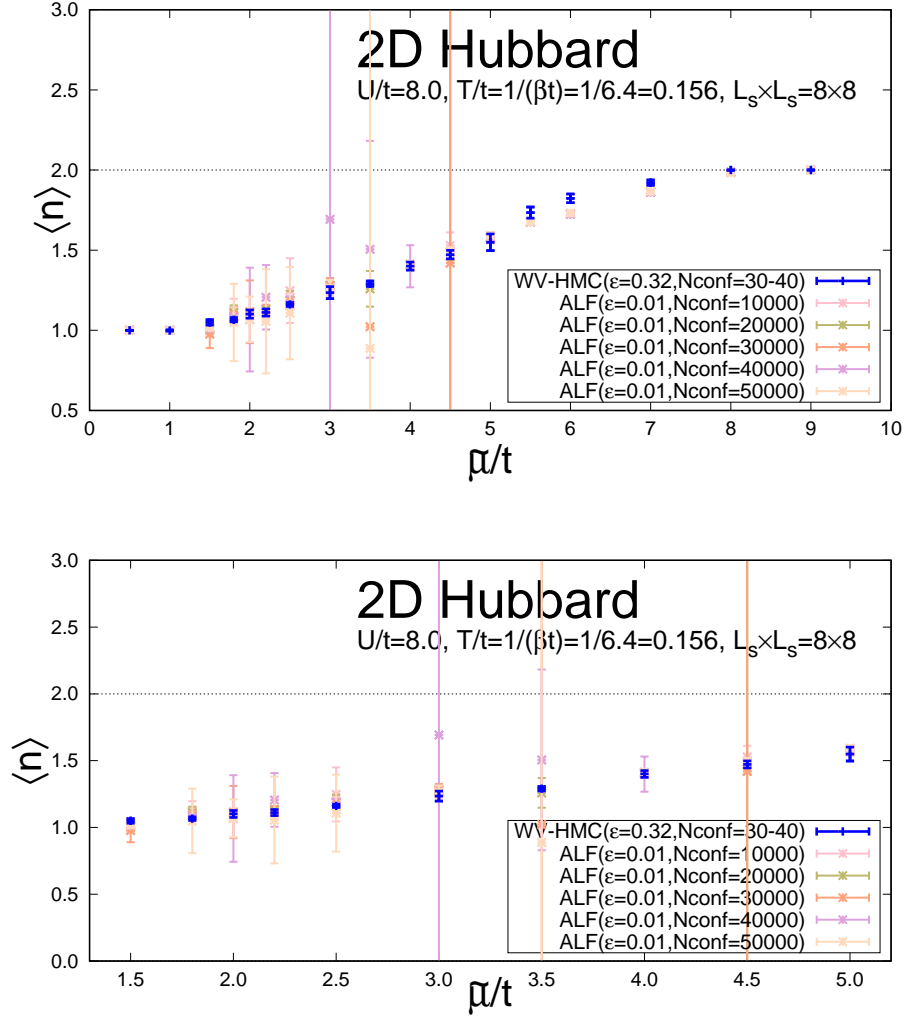


Figure 21: ($N_t \times L_s^2 = 20 \times 8 \times 8$) Number densities obtained using WV-HMC. ALF results are shown for comparison. Top: Full range of $\tilde{\mu}$. Bottom: Enlarged view of $1.5 \leq \tilde{\mu} \leq 5.0$, including ALF results with five different sample sizes.

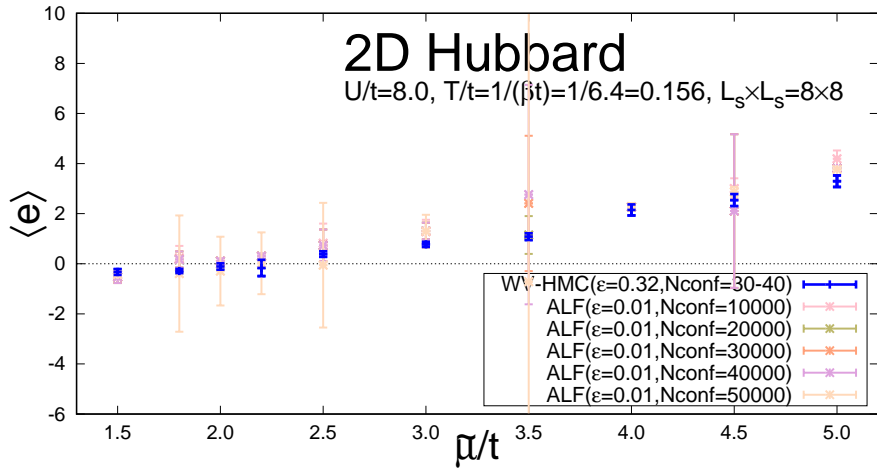
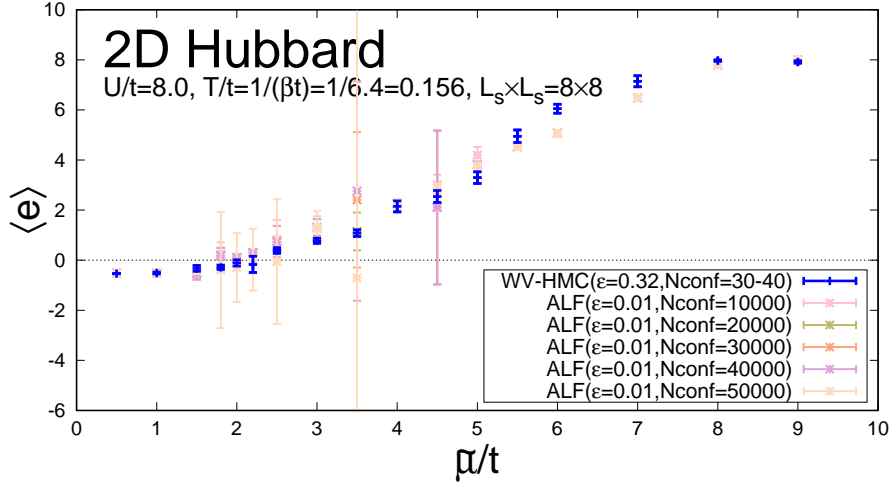


Figure 22: ($N_t \times L_s^2 = 20 \times 8 \times 8$) Energy densities obtained using WV-HMC. ALF results are shown for comparison. Top: Full range of $\tilde{\mu}$. Bottom: Enlarged view of $1.5 \leq \tilde{\mu} \leq 5.0$, including ALF results with five different sample sizes.